PERSISTENT REFLECTIVE OCEAN PARTICULATES OF BIOLOGIC ORIGIN: A GEOENGINEERING STRATEGY

by

John Matthew Nicklas

Submitted to Brown University in partial fulfillment

of graduation requirements for University Honors

in Applied Mathematics and Biology

May 2020

Co-Advisor: Charles Lawrence

Signature: _____

Co-Advisor: Baylor Fox-Kemper

Signature: _____

© Copyright by JOHN MATTHEW NICKLAS, 2020
All Rights Reserved

BROWN UNIVERSITY

APPLIED MATHEMATICS - BIOLOGY

DEPARTMENT APPROVAL

of a senior thesis submitted by

John Matthew Nicklas

This thesis has been reviewed by the research advisors and department chair. It has been found to be satisfactory.

Charles Lawrence, Co-Advisor

Baylor Fox-Kemper, Co-Advisor

Paul Dupuis, Department Chair

ACKNOWLEDGMENT

This work (principally the cost of computer simulations) is financially supported by a National Science Foundation grant awarded in part to Professor Baylor Fox-Kemper: Established Program to Stimulate Competitive Research (EPSCoR) and Rhode Island Coastal Assessment and Innovation Modeling (RI C-AIM) Cooperative Agreement Research Thrust 2 (RT2) (OIA #165521), "Predicting Ecosystem Response Through Integration". Professor Charles Lawrence is supported by NSF grant #1760838: "Collaborative Research: Bringing the Late Pleistocene into Focus: Better Estimates of Ages and Ocean Circulation Through Data-Model Comparison". Beginning in my freshman year and throughout my succeeding years at Brown, both of my advisors have provided exceptional encouragement and guidance in the development of this project.

This research was conducted using computational resources and services at the Center for Computation and Visualization, Brown University. Special thanks is given to Helen Kershaw for her invaluable help installing, running, and debugging CESM. Additional thanks is given to Drs. Keith Lindsay, Stephen Yeager, Alper Altuntas, and Jim Edwards for their assistance in troubleshooting errors.

As referenced later within the text of this thesis, I express my gratitude to Drs. Jay Brett and Zhonghai Jin for sharing their FORTRAN code regarding vertical particle advection and ocean radiative transfer respectively.

PERSISTENT REFLECTIVE OCEAN PARTICULATES OF BIOLOGIC ORIGIN:

A GEOENGINEERING STRATEGY

Abstract

by John Matthew Nicklas, Sc.B.
Brown University
May 2020

Advisors: Charles Lawrence and Baylor Fox-Kemper

This thesis project examines a novel method of geoengineering, a means to ameliorate the effects of anthropogenic climate change. As discussed in the first chapter of my thesis, solar radiation management (SRM) strategies reflect short-wave light, cooling the earth without reducing the atmospheric concentration of greenhouse gases. The SRM strategy explored in this thesis uses reflective biological particles that float on the ocean's surface and accumulate in the subtropical gyres. Coccolithophores are identified as candidate organisms for generating these reflective particles, but my further investigation of this geoengineering strategy does not depend on any specific properties of these microorganisms. In the second chapter of this thesis, I modify the CESM fully-coupled global climate model to simulate all aspects of this intervention, including the advection of the particles and their optical properties. I then examine three modified CESM simulations which approximate the regional climate effects of ocean SRM geoengineering. In the third and final chapter of my thesis, I develop a statistical approach for filtering the global climate temperature. This climate temperature was previously calculated as a 30-year moving average, a definition that implies that the current climate is unknown. However, using a Kalman filter with dynamic equations derived from basic radiation physics, I separated the annual gaussian noise uncertainty in temperature (weather) from the climate temperature uncertainty. This approach can be generalized to analyze many additional variables (such as precipitation). Kalman filters thus discern the effects of geoengineering in real time, allowing control algorithms to react and adjust the ocean intervention within the CESM model.

TABLE OF CONTENTS

Page

ACKNOWLEDGMENT iii

ABSTRACT iv

LIST OF FIGURES vi

LIST OF TABLES vi

CHAPTER

1 Introduction to Ocean Geoengineering 1

1.1 Current Physical and Research Climate 1

1.1.1 Need for Intervention 1

1.1.2 Moral Imperative vs Moral Hazard 2

1.1.3 Reflective Stratospheric Aerosols: Many Side Effects 3

1.2 Reflective Ocean Particles: An Improvement 4

1.2.1 Biologic Basis and Feasibility 5

CHAPTER

2 Simulation: CESM Changes 8

2.1 Prior Work 9

2.2 Flotation: Convection-Diffusion 12

2.3 Heat Flux at Ocean Surface 14

2.3.1 COART Model 15

2.4 Growth and Decay 17

2.5 Underlying Model Specifications 17

2.6 Preliminary Results from Geoengineering Simulations 18

CHAPTER

3 Statistical Filtering 24

3.1 Kalman Filtering, Smoothing, and Extensions 24
3.2 Weather as a Noisy Climate Signal 26
3.2.1 Derivation of Dynamic Equation 28
3.2.2 Completion of EKF 33
3.3 Initial Results on Historical Data 36
3.3.1 MCMC Variation of Parameters 40
3.3.2 Comparison with CESM LENS Ensemble 43
3.4 Future Work: More Variables and Control Theory 46

APPENDIX

A 48
A.1 Glossary of Symbols 48
A.2 Potential (Commercial) Benefits 49

B 50
B.1 Buoyancy Simulation - Simplified Example 50
B.2 Numerical Scheme of Advection-Diffusion 51
B.3 COART Emulator 53

C 58
C.1 Derivation of LOG[CO2] 58
C.2 Core Kalman Filter Code 59

REFERENCES 47

LIST OF FIGURES

1.1 Global CO_2 Emissions with linear trend 2

1.2 Prior floating particle simulations 4

1.3 Coccolithophore electron micrograph 6

2.1 Uniform ocean surface albedo increase of +0.03 10

2.2 Ocean surface albedo increase correlated to shipping traffic 10

2.3 G1 experiments (+0.06 to +0.15) of uniform ocean albedo increase 12

2.4 Southern ocean gyres albedo increase of +0.07 13

2.5 Buoyancy demonstration of average particle concentration with depth 14

2.6 Modeled buoyant particle accumulation in ocean gyres 15

2.7 Albedo output of COART and emulator 16

2.8 Absorbance output of COART and emulator 17

2.9 Overall geoengineering impact on surface temperature 19

2.10 Regional impact on surface temperature 20

2.11 Acceleration of meridional overturning circulation 21

2.12 Total absorbed light by ocean region 21

2.13 Geoengineering effects on precipitation 22

2.14 Geoengineering effects on phytoplankton - May 23

2.15 Geoengineering effects on phytoplankton - November 23

3.1 T from HadCRUT4 vs. the $_{30} < T >$ climate temperatures 27

3.2 Distribution of deviations of T from $_{30} < T >$ 28

3.3 Correlation between $\log [CO_2]$ and back-scattering 29

3.4 Blind model performance vs. $_{30} < T >$ 33

3.5 Graph of the model state update equation, which is roughly linear 35

3.6 $_{30} < T >, T$, blind model, EKF state estimate, and RTS state estimate . . . 37

3.7 EKF forward posterior vs. T 38

3.8 Distribution of EKF innovation residuals 38

3.9 RTS-smoothed estimate compared to $_{30} < T >$ 39

3.10 Distribution of differences between the RTS-estimated state and $_{30} < T >$ . . 40

3.11 MCMC score evolution over 5000 samples 41

3.12 Parameter evolution throughout MCMC search 42

3.13 LENS hind-cast simulation spaghetti plot 44

3.14 Kalman filter predictions vs LENS hind-cast simulations 45

B.1 First interpolation for albedo of COART emulator 54

B.2 Second interpolation for albedo of COART emulator 55

C.1 Outgoing radiation emission spectra with various CO_2 concentrations 60

LIST OF TABLES

3.1 Values of fitted coefficients in blind model 33

3.2 Correlations between MCMC-sampled parameters 43

A.1 Glossary of mathematical symbol meanings 48

Dedication

This thesis dissertation is dedicated to my mother, father, and sister
who provided immeasurable support and encouragement,
and also to my grandmother Beryl Shelley Nicklas
who studied her way off of a mountain.

Chapter One

Introduction to Ocean Geoengineering

1.1 Current Physical and Research Climate

1.1.1 Need for Intervention

Conventional means to prevent anthropogenic climate change increasingly appear insufficient. (Olhoff and Christensen, 2019) Despite the complexity of economic models envisioning future emissions scenarios, the growing annual global anthropogenic CO_2 emissions are incredibly well explained by a linear fit (R^2=0.98 see Figure 1.1). Since the Kyoto Protocol in 1998, despite increased awareness and investment in renewable energy, actual greenhouse emissions have overtaken this linear interpolation. Carbon sequestration technologies (most promisingly direct air capture) currently exist only as working small-scale prototypes. Therefore, although the most recent IPCC Report (Masson-Delmotte et al., 2018) concluded that 45% emissions reductions are needed by 2030 to keep global warming to below 1.5°C, these scenarios are exceedingly improbable. This research focuses on developing a novel treatment for the problem at hand: a way to mitigate the effects of elevated CO_2 on the climate system. Unlike in medicine, I do not have the luxury of complete physical experimental systems to test climate treatments. In lieu of that impartial approach, I herein utilize the next best tools to assess my proposed treatment: both dynamical/mechanistic modeling and statistical modeling (Rougier and Goldstein, 2014).

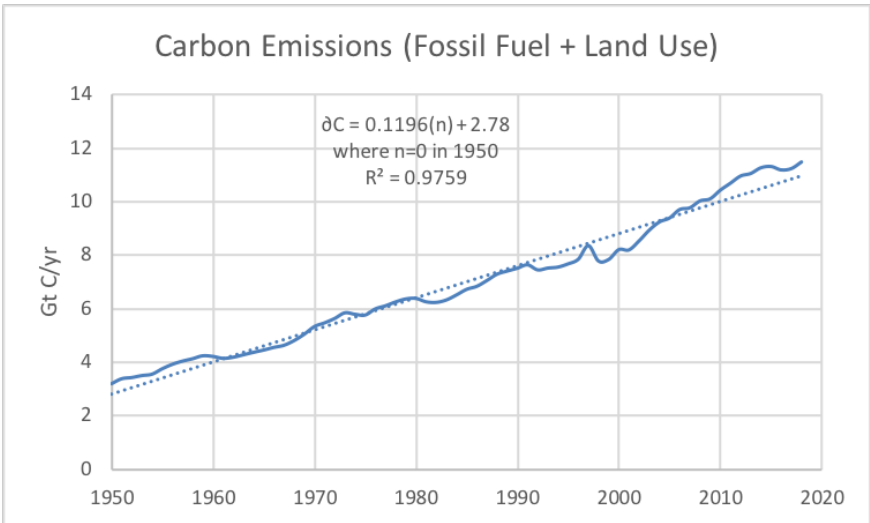

Figure 1.1 Global carbon emissions spanning from 1950 to 2019. The dashed line is the linear fit, from which the real emissions in solid blue never deviate by more than 0.74 Gt. (Friedlingstein et al., 2019). Note that the mass of CO_2 is 3.664 times the mass of emitted carbon, and the atmosphere has volume such that each Gt of emitted carbon increases the $[CO_2]$ by roughly 0.25 ppm.

1.1.2 Moral Imperative vs Moral Hazard

In the absence of an available cure, a moral physician must make all attempts to reduce pain, which is often practiced by managing symptoms (Carvalho et al., 2018). Applying this concept to climate science, it is our moral imperative to reduce the affects of climate change even if we cannot address the root cause. Within climate change literature, such alleviating efforts are termed "adaptation". I believe that a deliberative physician-patient framework (E. J. Emanuel and L. L. Emanuel, 1992), with its emphasis on informed consent, is the best context from which to evaluate non-curative treatments for anthropogenic climate change, termed geoengineering. This stance is directly opposed to that termed "moral hazard", in which serious consideration of geoengineering is discouraged because such discussion might detract from the political and economic impetus to reduce carbon emissions (Lin, 2013). This "moral hazard" approach is implicitly paternalistic. True respect toward patient autonomy (and by extension, established means of governance) is predicated on the assumption that

individuals are capable of weighing complex choices and can understand the conceptual distinction between permanent risk reduction and perennial treatment. We must endeavor to offer both: carbon reduction and safe mitigation.

Along similar lines, the implementation of emissions reductions to lessen climate change has become a highly charged political issue. Limited evidence shows that discussion of geoengineering does not impact any citizen's opinion toward emissions reductions (as this stems from their core worldview), but does increase trust in climate science among conservatives (Fairbrother, 2016). If a patient is averse to a particular treatment, a deliberative doctor can build trust by discussing other treatments.

1.1.3 Reflective Stratospheric Aerosols: Many Side Effects

One technologically feasible means to suppress the effects of global warming is to loft reflective aerosols into the stratosphere, which would cool the earth by reducing the intensity of incoming shortwave light (Keith et al., 2016). However, this treatment would bring inherent side effects: variegated alteration of regional precipitation and temperature, human respiratory disease caused by aerosols, reduction in performance of crops, solar panels, and telescopes worldwide to list a few (Robock, 2008). The stratospheric aerosol treatment requires unpalatable preconditions: continuous aerosol dosing must be ensured, and global effects will require consent of all sovereign nations to a single SRM plan. Should this form of geoengineering cease, the climate system will rebound to nearly its CO_2 equilibrium state (the climate that would have existed without any SRM intervention) within 5 years. (Parker and Irvine, 2018; McCusker et al., 2014) The consequences of such a "termination shock" would be absolutely catastrophic, more so than even the current rate of warming, as populations and ecosystems would not have no time to react to their changing climate.

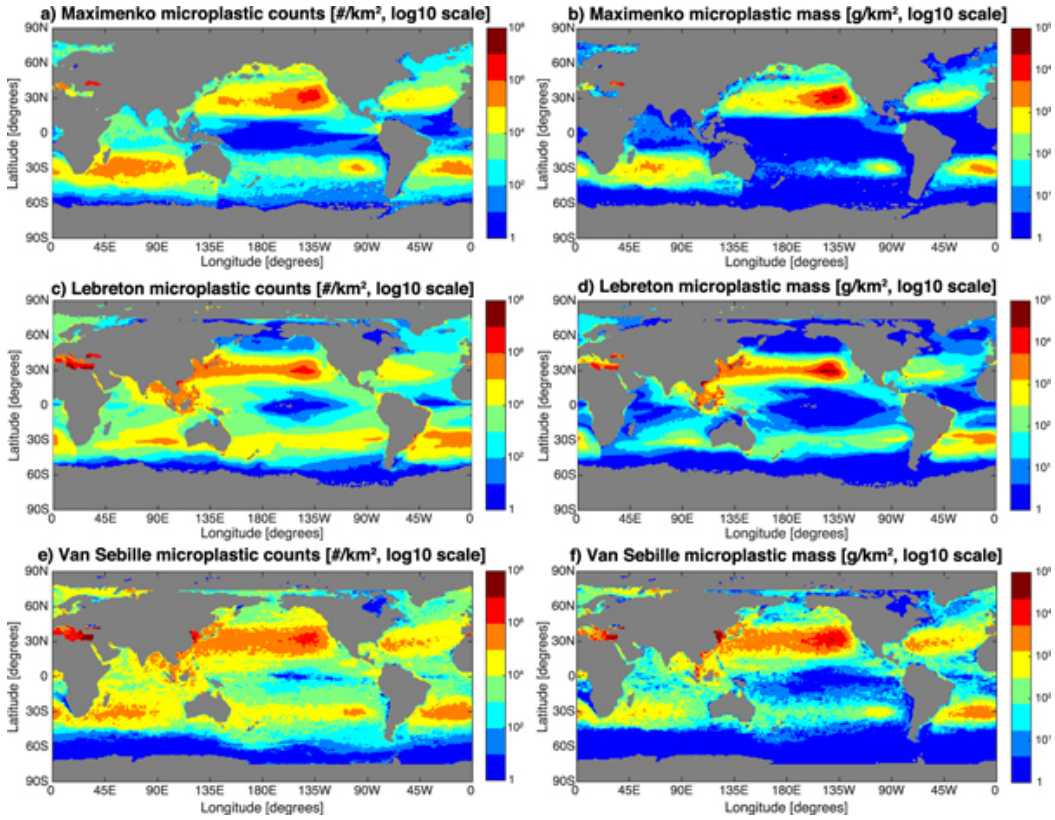

Figure 1.2 Comparison of 3 simulations of ocean plastic distribution over multiple decades. My beneficial floating particles will accumulate within the climate model in a similar manner. (Sebille et al., 2015)

1.2 Reflective Ocean Particles: An Improvement

An alternative treatment would generate a stable, nearly permanent reflective substance at the surface of the ocean (Seitz, 2011; Evans et al., 2010), which would accumulate in the subtropical ocean gyres on a timescale of decades (Sebille et al., 2015) (see Figure 1.2) and be maintained by an autonomous artifical ecosystem. This ramp-up timescale of decades entails different risks than the 1-2 year timescale for utilization of stratospheric aerosols (Hall and Waugh, 1997), and especially the 1-2 week timescale (and air quality health risks) of tropospheric aerosols (Pan et al., 2016). This would exchange many of the global side effects of stratospheric aerosols for more manageable local concerns, such as potential damage to aquatic ecosystems. Of note, these subtropical and oligotrophic deep ocean ecosystems which

such a scheme may put at risk are among the least ecologically productive and are growing in size (Polovina, Howell, and Abecassis, 2008). This treatment has been incompletely explored within computer models: it has been simulated by uniformly increasing the albedo of the entire ocean (Kravitz, Rasch, et al., 2018), by regionally increasing the albedo based on a static map of cargo shipping traffic (Crook, Jackson, and Forster, 2016), and most resembling what I shall attempt, by using static boxed regions overlaying the southern hemisphere gyres (Gabriel et al., 2017). In Chapter 2, I demonstrate my methods for a more rigorous simulation of this geoengineering strategy using the Community Earth System Model (CESM), which captures both reflective particles' motion due to and their simultaneous effect on ocean circulation, as well as impacts on oceanic biogeochemistry (via a model of the primary aquatic producers and consumers). In Chapter 3, I develop a statistical Kalman Filter control theory framework for climate models. This statistic framework will allow me to assign probabilities to the benefits (reduction of surface temperature) and potential adverse side effects (changes to precipitation patterns and to the ocean ecosystem).

1.2.1 Biologic Basis and Feasibility

While this choice has little affect on the following simulation, I propose that a modified species of coccolithophore would be ideal to generate the desired reflective particles. Coccolithophores are abundant throughout the global oceans and can be easily cultured (Geisen et al., 2004). Cocoliths, the microscopic scales protecting these unicellular eukaryotes are reflective, enough to contribute 0.13% to Earth's albedo, and cause local increases of albedo by over 5% (Tyrrell, Holligan, and Mobley, 1999). Calcium carbonate persists above the saturation depth (including the surface), and this will remain true despite projected ocean acidification (Zheng and Cao, 2014). The mass of material that is chemically available to calciferous organisms is on the scale of Pg, even if I only include $[CO_3^{-2}]$ within the volume of water projected to have supersaturated $[CaCO_3]$ in 2100 under

the most severe emissions projections (and thus augmented ocean acidification). Beyond a means to cover a vast area of water (at least several million square kiometers), the rough and corrosive conditions of the ocean surface are a significant engineering constraint for any ocean geoengineering schemes, as even relatively tough buoyant plastics are rapidly digested from larger structures into millimeter-sized chips (Morét-Ferguson et al., 2010). Any factory-made cohesive structure is ridiculously impractical. But the past 50 years have brought tremendous progress in bioengineering (especially of microorganisms). The genetic code can be read with next-generation sequencing (Kulski, 2016), modified with CRISPR (Adli, 2018), or even expanded to code for unnatural proteins (Y. Zhang et al., 2017).

To modify a representative coccolithophore, say *Emiliania huxleyi*, to fit the role proposed in this thesis, two changes would have to be made: buoyancy and apoptotic self-embalming. To make these microorganisms positively buoyant such that they are not lost below mixed layer by diffusion, I propose transgenically inserting gas vacuole proteins, such as found in *Microcystis aeruginosa* (Jones and Jost, 1971). More complex changes would be necessary to induce the genetically modified organism to seal its spherical shell upon programmed cell death. For this purpose, I propose a screen to selectively mutate the genes involving $CaCO_3$ deposition. In this screen, coccolithophores will be grown in a viscous media so that colonies cannot spread far from the original clonal cell, then upon apoptosis the dying clonal cell releases a transgenic toxin killing all of its descendants, unless the living or dying cell can find a way to seal off the coccoliths into a sphere. The resulting product will be, in essence, a floating fossil that can persist independently of the culture of coccolithophores.

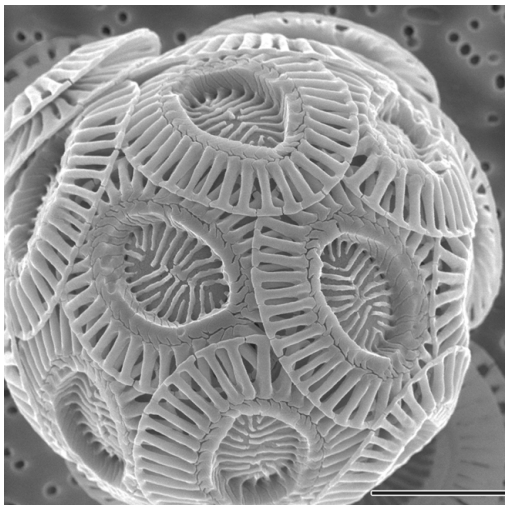

Figure 1.3 Electron micrograph of *Emiliania huxleyi* shown, the most common species of coccolithophore. Image credit to (Taylor, 2011)

Chapter Two

Simulation: CESM Changes

CESM (the Community Earth Systems Model) is a state-of-the-art, fully-coupled climate model that critically encompasses atmospheric, ocean, and ice model simulations. Therefore, CESM allows for all aspects of this floating reflective particle scheme to be simulated: the accumulation of particles to the subtropical ocean gyres, the local and global effects of the heat reflected away as shortwave light, and any feedback that these major climate changes may have on the particles' transport. This model has good capability to predict core meteorologic variables such as temperature, cloud fraction, and precipitation (He et al., 2015), in addition to the essential ocean variables such as current, salinity, and thermocline (relative to observations) (Danabasoglu et al., 2012). While this model is currently unable to resolve such mesoscale features as ocean eddies and individual storms, well-studied paramaterizations are used to capture the effects of these unseen features (Gent and Danabasoglu, 2011). Also, many variables of lesser importance may retain bias (He et al., 2015).

This geoengineering scheme primarily involves modifications to the ocean component of CESM version 1.1, POP2 (the Parallel Ocean Program) (R. Smith et al., 2010). Additionally, the results of a large ensemble (LENS) containing many dozen simulation replicates is utilized as a control (Kay et al., 2015).

2.1 Prior Work

A few teams of researchers have previously simulated similar ocean geoengineering interventions, although none before this work display dynamic variations in the changed albedo. The majority of these experiments (and mine) combine a geoengineering scheme with some potential representative concentration pathway (RCP) that envisions a future trajectory of greenhouse gas concentrations. Within the geoengineering intercomparison project (GeoMIP), such experiments are named G4 (Kravitz, Robock, et al., 2013).

Crook et. al. simulated two different kinds of ocean geoengineering interventions with the HadGEM2-CCS model (a peer of CESM) on the background of the RCP4.5 greenhouse emissions projection (Crook, Jackson, and Forster, 2016). In one experiment, named G4 Uniform, the surface of the ocean was uniformly changed to have an albedo of 0.10 rather than 0.07 (see Figure 2.1). In a second experiment, the areas of ocean containing the major routes of ocean cargo vessels were changed to have a substantially higher albedo according to the volume of traffic (see Figure 2.2). This second experiment was named 'G4 Shipwake' because it attempts to capture the effects of generating reflective microbubbles in the wakes of large watercraft which could persist for days (Seitz, 2011). The uniform change of increasing the albedo by 0.03 yielded a global cooling of 1.6K, whereas the Shipwake experiment was only a third as potent, yielding a decrease in temperature by 0.5K. Regionally, both of these experiments demonstrated substantial cooling in the Arctic (by up to 10K) and marginal cooling in the tropics (by 1-2K). However there was uncertainty regarding whether cooling would occur in the Southern Ocean and the North Atlantic region.

Another paper by Kravitz et. al. examined a uniform application of simulated albedo geoengineering, a very similar intervention to the aforementioned G4 Uniform experiment (Kravitz, Rasch, et al., 2018). This analysis combined results from 11 comparable coupled climate models, and the experimental design was quite different. All simulations combined in this paper simultaneously implemented A) an instantaneous quadrupling of CO_2 to over

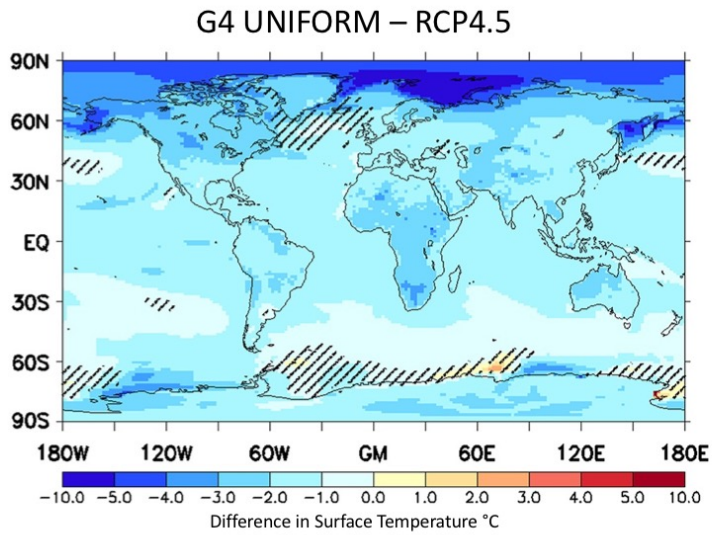

Figure 2.1 Simulated uniform albedo increase by +0.03 over the entire ocean surface. Hashed sections indicate uncertainty compared to the RCP4.5 background. (Crook, Jackson, and Forster, 2016)

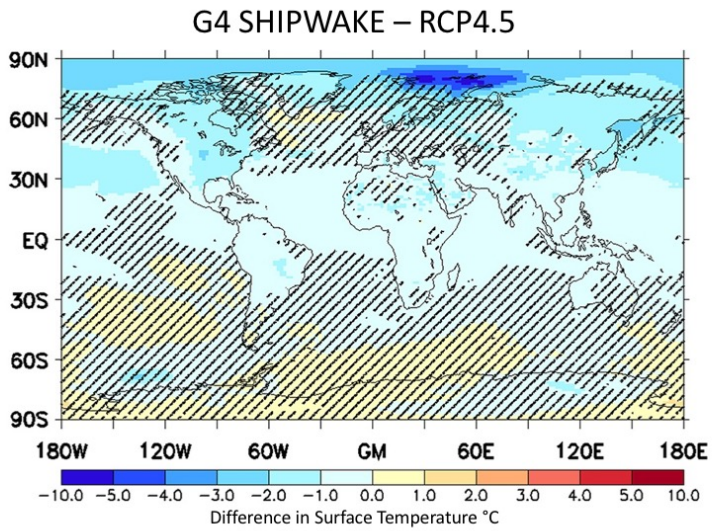

Figure 2.2 This simulated alternative method of making the ocean more reflective involves infusing ship wake with surfactant to make microscale bubbles. The intervention was weighted to the northern hemisphere because there is more commercial shipping traffic there. (Crook, Jackson, and Forster, 2016)

1100ppm, a greenhouse gas concentration that would only be achieved after 2080 in the most severe RCP8.5, and B) a uniform increase of ocean albedo to a sufficient level that the top-of-atmosphere radiation is balanced (this ensures that no net heating occurs in the climate system). To achieve this result, some of the models had to increase the ocean albedo by a factor of 2.4 (from 0.09 to 0.23) whereas others required a much more modest change (from 0.12 to 0.17). As can be seen in Figure 2.3, there is agreement between models that cooling will occur in large parts of the tropical oceans, whereas warming results over most land areas and in the poles. These results appear to directly contradict those observed in the G4 Uniform experiment. Perhaps polar sea ice enhances the cooling effect of a slightly more reflective ocean under low concentrations of greenhouse gas, but with higher greenhouse gas concentrations and corresponding larger albedo changes, most polar sea ice disappears and the most cooling occurs where there is more light to be reflected away, at the tropics.

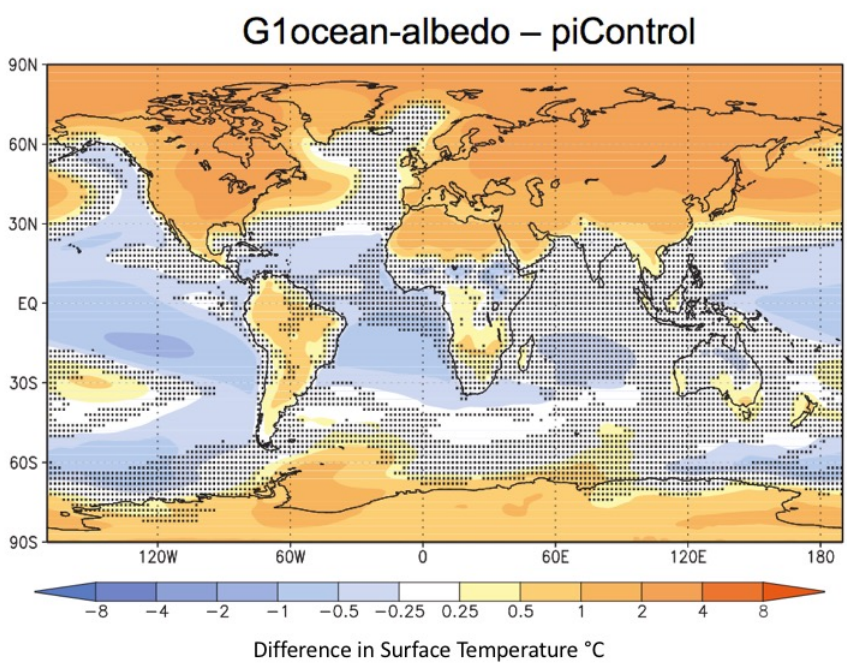

Figure 2.3 This is a compilation of 11 G1 experiments - the temperature of the climate system does not change by design, because the ocean albedo has been augmented up to match a 4x jump in CO_2 while keeping heat flux constant.(Kravitz, Rasch, et al., 2018)

Lastly, the findings of Gabriel et. al. most closely mimic what I will simulate in this paper, albeit in a fixed and crude manner. (Gabriel et al., 2017) Recognizing that reflective particles will concentrate in ocean gyres, the authors of this paper simply boxed in several of these regions and specified that the albedo within these boxes would be increased from 0.06 to 0.15. Because mitigation to climate change will be most critical in the global south, the three southern ocean gyres were chosen, and it was assumed that particles would not cross the equator due to the intertropical convergence zone. This G4 experiment was conducted on a slightly more severe greenhouse emissions background (RCP6) than work of Crook et. al., but less severe than quadrupling of carbon in the G1 experiments. As Figure 2.4 demonstrates, the albedo change induced the greatest drop in temperature immediately on top of the ocean gyres and in the Southern Ocean. Additional cooling effects were present throughout the southern hemisphere and in the Arctic, but statistically significant warming also occurred east of Japan.

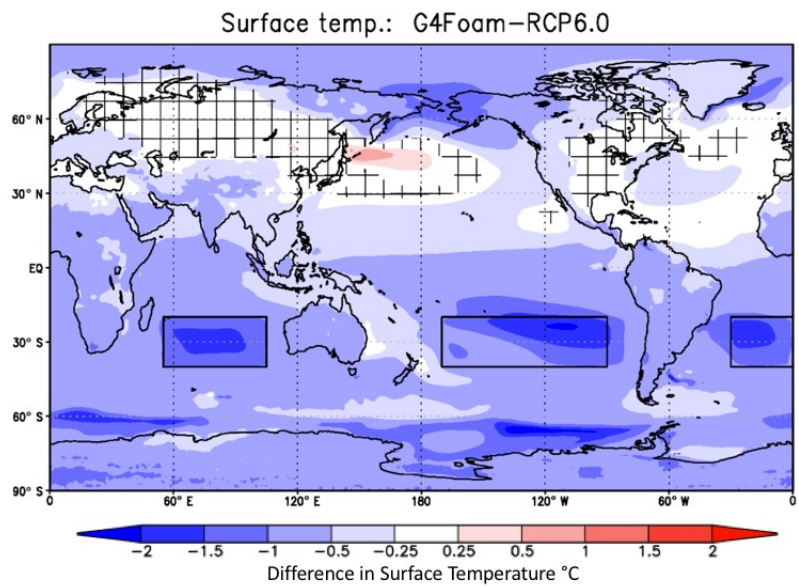

Figure 2.4 Simulated albedo increase of +0.07 within the boxed regions encapsulating the three southern ocean gyres. Most cooling occurs in the southern hemisphere, but distant effects are also observed in the northern hemisphere. (Gabriel et al., 2017)

2.2 Flotation: Convection-Diffusion

Buoyant particulates of any size will move up in the water column, and they will also spread out vertically by diffusion. This simulation is implemented as a variation on the explicit advection-diffusion difference approximation, and is given more rigorous treatment in Appendix B1. Both this implemented buoyancy scheme and the existing discrete tracer transport equations (R. Smith et al., 2010) are implemented as linear differential operators in space, which are first-order accurate in time. The positional change from all of these operators is added together to generate the overall particle movement. By Theorem 4.3.1 of Time-Dependent Problems and Difference Methodsn(Gustafsson, Kreiss, and Oliger, 2013), the approximation schemes of each of these operators may be implemented sequentially at each time step. Due to the buoyancy affecting only the introduced reflective particles, this advection-diffusion scheme is implemented in a distinct section of code (namely cfc_mod.F90) from the schemes which affect all tracers. Similar work has simulated sinking biological tracers (Brett et al., 2020).

Within this simulation, the particles are given a rise velocity of 5 m/day. This rate is comparable to the sinking velocity of coccolithophores, (H. Zhang et al., 2018) and larger rise velocities give rise to numerical instabilities in low-resolution models. This rise velocity (examined in the advection-diffusion scheme in Appendix B1.2) means that a large portion (30%) of the buoyant particles remain in the top layer (10 m) of the model, whereas for control neutrally buoyant particles, only about 5% of the particles remain in the top layer. Over 60% of buoyant particles but only 15% of neutral particles are contained within the top 30 m of ocean. This concentration is plotted with respect to depth in Figure 2.5. Furthermore, the combination of this buoyancy scheme with the ocean currents already computed in CESM yield the expected accumulation of buoyant particles at the surface in the aforementioned subtropical ocean gyres (see Figure 2.6).

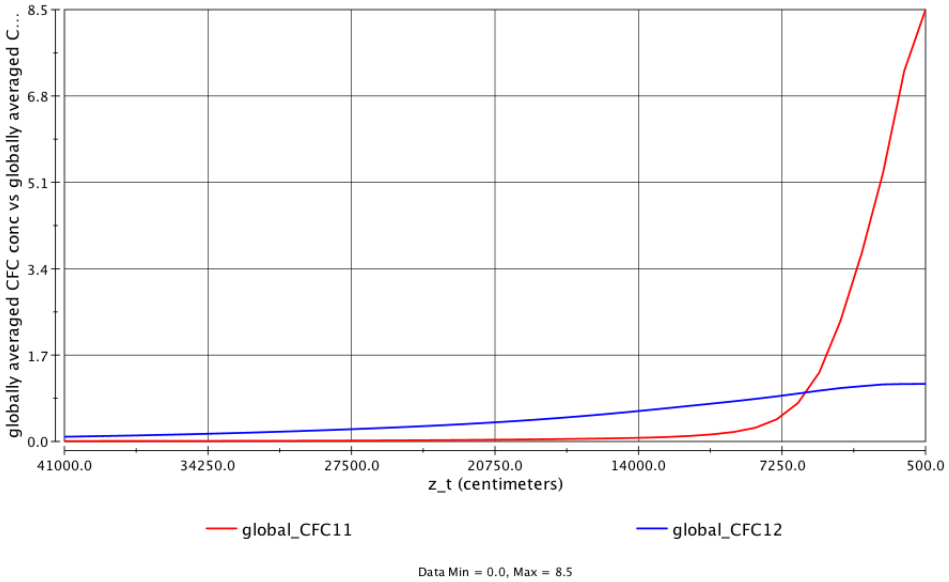

Figure 2.5 The averaged concentration of buoyant particles (labeled CFC11 in red) and non-buoyant control particles (labeled CFC12 in blue) are plotted across ocean depths. These concentrations do not add up to the same total because the buoyant particles are both being added to the ocean surface in a greater quantity than the control particles and decaying at a constant rate, whereas the control particles do not decay.

2.3 Heat Flux at Ocean Surface

Within the overall CESM architecture, ocean albedo was originally computed in the driver (aka coupler for v2), taking 6 inputs of both visible and near-infrared energy down-welling fluxes for light that is diffuse, direct, and has passed through ice. The original algorithm just summed these and multiplied by a function of the sun's azimuth angle $\cos z$ to yield the ocean-warming radiative flux. Instead, I modified the code such that the visible and near-infrared lights were summed within the driver and passed to the ocean model as direct, diffuse, and ice-penetrating light. From there, those components were taken as inputs to a custom-built COART emulator, which would yield both A) the amount of light that passes into the ocean and will be absorbed as heat, and B) the amount of light absorbed in the top 10 m of the ocean (as real-world reflective particles absorb light too).

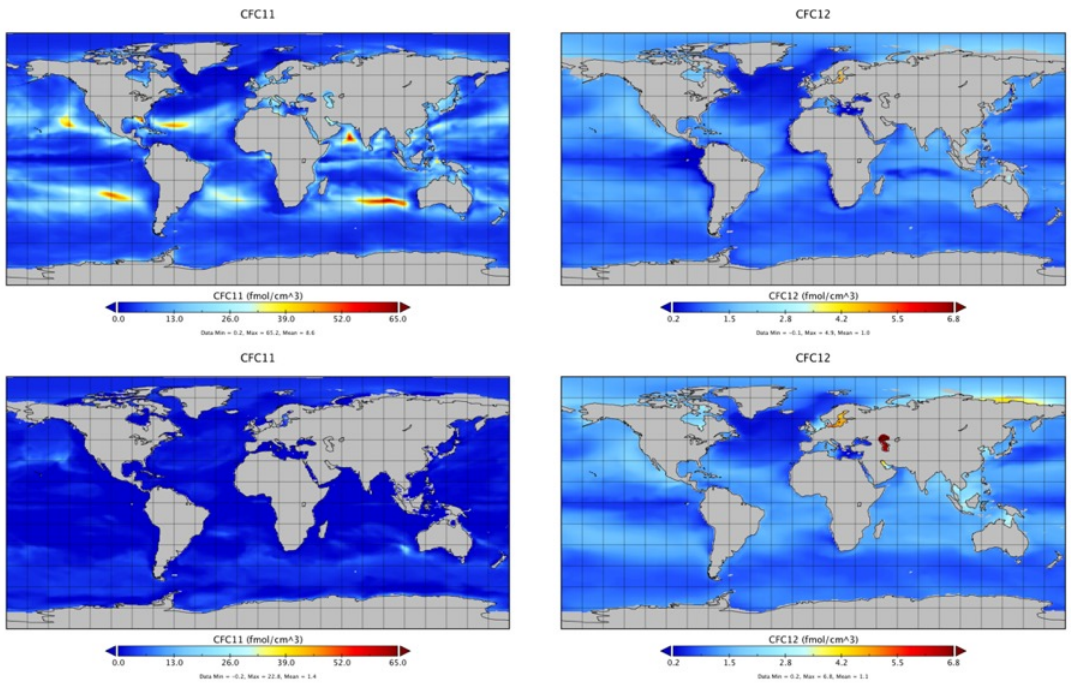

Figure 2.6 The following figures demonstrate that this flotation method works. They show the concentration of buoyant particles (left) and non-buoyant control particles (right) at both the top 10 m of the ocean (above) and 40-50 m below the surface (bottom). Clearly, the buoyant particles are accumulating on the ocean surface in the ocean gyre regions. Please excuse the differences in concentrations - in this particular run the total amount of control particles has been added at a rate only 0.1 times that of the buoyant particles, but the color bars have been scaled appropriately.

2.3.1 COART Model

These 3 inputs are then passed to a custom built-to-purpose emulator of the COART model (Jin, Charlock, Rutledge, et al., 2006), based on a series of over 1500 computations from the COART online model over the range of expected values. Unfortunately, prior computed tables did not include such unnaturally high concentrations of reflective particles in the water (Jin, Charlock, W. L. Smith, et al., 2004). This emulator uses a particle scattering coefficient of the water b, a total chlorophyll concentration Chl (both real chlorophyll and additional pigment produced by the organic particulate-makers), and the angle of the sun for direct light. Diffuse light is assumed to have an angle $\cos z = 0.67$, and wind (velocity squared) is

also accounted as an additional boost to the albedo (Jin, Qiao, et al., 2011). Ice-penetrating light was simply deposited as energy below the first layer of the ocean. See Appendix B2 for a detailed mathematical description of this emulator, which is in essence a series of nested interpolation functions.

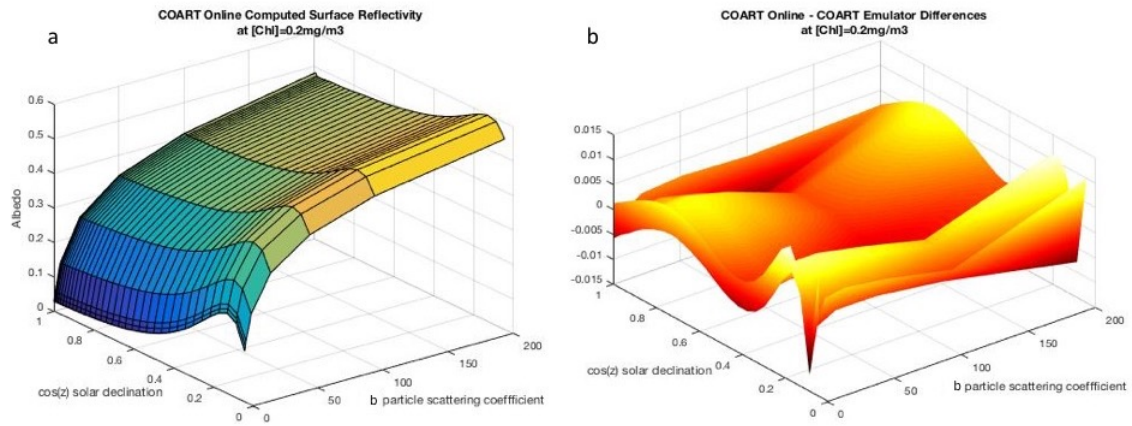

Figure 2.7 Albedo outputs of the COART Online and Emulator Differences. Note that this function lives in more dimensions than can be plotted - these are the values with [Chl]=0.2 (Jin, Charlock, Rutledge, et al., 2006)

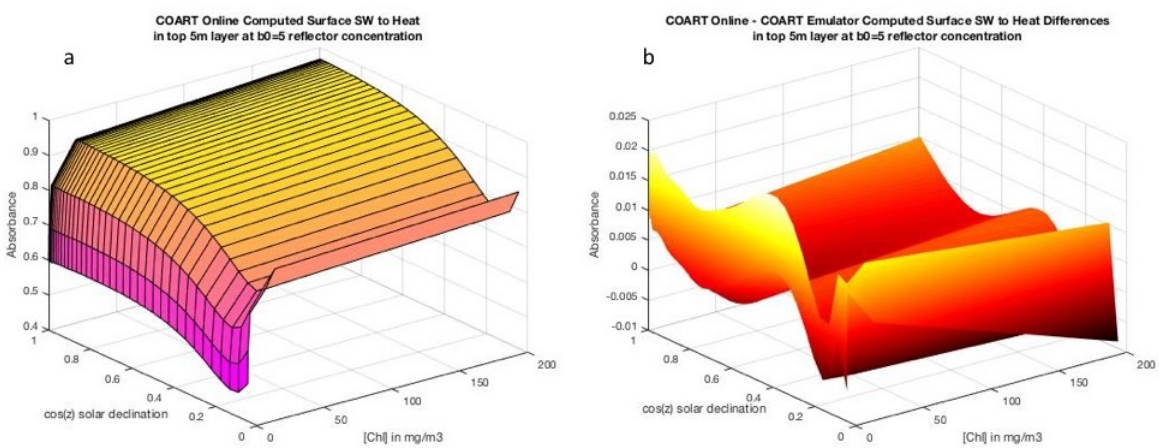

Figure 2.8 Absorbance outputs of the COART Online and Emulator Differences. Note that this function lives in more dimensions than can be plotted - these are the values with b=5 (Jin, Charlock, Rutledge, et al., 2006)

This custom emulator was developed both because the COART code itself did not run

with the required CESM FORTRAN compilers, and this algorithm may likely be too slow to run within the model (at each timestep, at each grid point). However, my emulator is accurate in albedo to within an error margin of <1% in 98% of tested cases, and in top-layer absorption in 73% of tested cases. This emulator never has a point error exceeding 5% for either albedo or absorption. Below the top layer, everything is calculated as it was originally within the CESM.

2.4 Growth and Decay

Growth only occurs on the surface, through a user-defined input field. Particles currently have a half-life decay of 1 year and are grown uniformly over the Earth's surface. Simulation results indicate that while such particles will temporarily accumulate in the subtropical gyres, this accumulation is seasonal (occurring only in the summer). This suggests that a half-life of 1 year is too short for these reflective particles to maintain a permanent reflective area.

I plan to conduct experiments in which growth only occurs at the mouths of major eutrophication-prone rivers in a follow-up experiment, as this is expected to produce a slightly different distribution of reflective particles. Preliminary results indicate that the 1 year half-life is too short for the particles to migrate from river deltas to the subtropical gyres.

2.5 Underlying Model Specifications

CESM1.1 was run with CAM5 atmosphere and ocean biogeochemistry. The resolutions used were 0.9x1.25 degree spherical grid for atmosphere and land models, gx1v6 ice and ocean grids (334x320 cells, 60 level depths, displaced pole). The atmosphere, land, and ice models had an half-hour time step, whereas the ocean had an hourly time step. Carbon dioxide emissions followed the business-as-usual RCP8.5. See LENS (Kay et al., 2015) for details.

2.6 Preliminary Results from Geoengineering Simulations

Following the GeoMIP G4 protocol (without termination), experiments were started in 2020 and run through 2089 under a background context of RCP8.5, the most severe, business-as-usual emissions scenario. While more experiments are ongoing, three are examined in this thesis: a control run, a maximal intervention experiment (in which global cooling exceeded the effects of greenhouse emissions), and a minimal intervention experiment (in which global cooling offset a small portion of the warming from greenhouse emissions). The overall temperature changes are shown in the plot below (Figure 2.9).

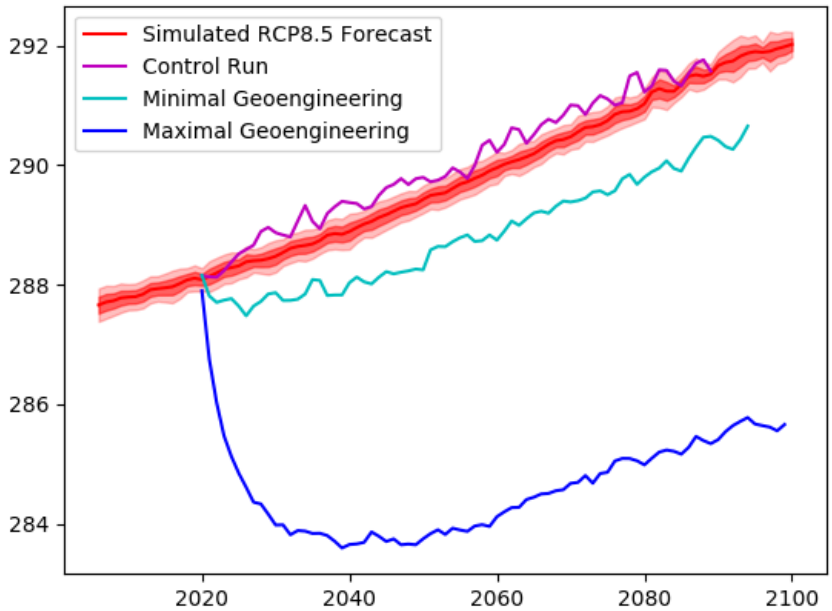

Figure 2.9 Time series of averaged global surface temperatures from the three geoengineering simulations compared to the LENS RCP8.5 forecasts (gradations in red shading correspond to 1σ and 2σ). The control simulation is slightly warmer than the ensemble forecast because it uses a different (COART-based) computation of reflection and absorbance. The minimal geoengineering experiment reduces global temperature by about 1.3K. However, the maximal geoengineering experiment more than compensates for the greenhouse gas emissions (a cooling equal in magnitude to those seen in historical ice ages).

Regarding the regional changes in temperature, there was remarkably uniform cooling in both the minimal and maximal geoengineering experiment (see Figure 2.10). In particular, cooling was not concentrated in the tropics as was observed in atmospheric SRM experiments. Warming was observed the Northwest Atlantic ocean, but this result is expected due to a substantial acceleration of the meridional overturning circulation (see Figure 2.11).

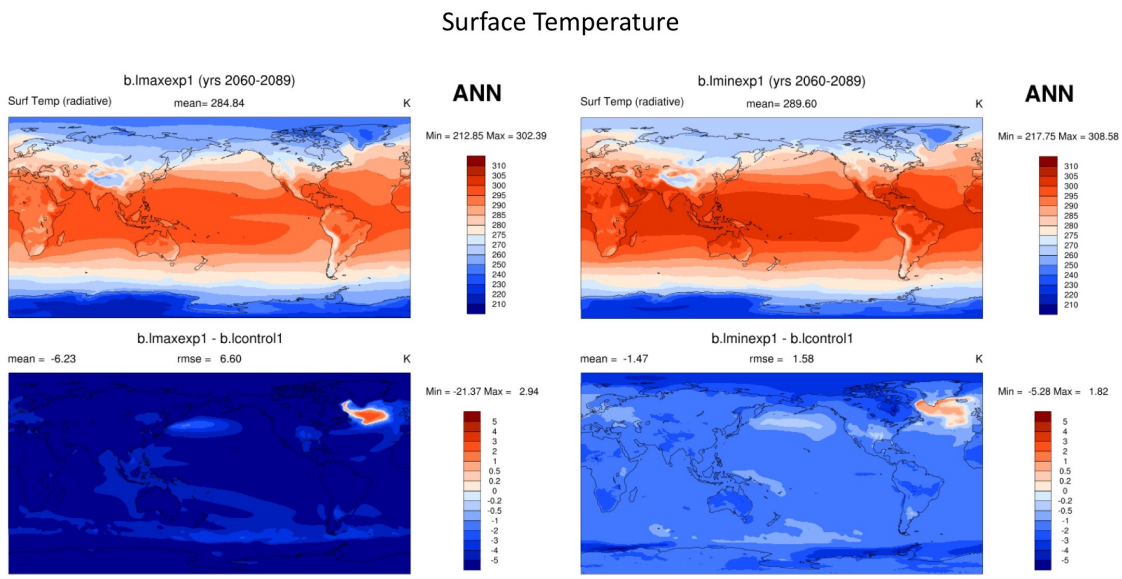

Figure 2.10 The ocean particle geoengineering strategy is simulated to have roughly uniform impact on surface temperature relative to the RCP8.5 control run, except for the Northwest Atlantic Ocean. As will be true for the subsequent figures (2.10-2.15), the top row of maps corresponds to the absolute temperatures observed in the two geoengineering experiments, whereas the bottom row corresponds to the differences between these experiments and the control run. The maximal intervention experiment maps are on the left and the minimal intervention maps are on the right. Figures 2.10-2.13 are 30-year averages.

The direct effects of the changes to ocean albedo can be observed in the differences in the heat from shortwave light flux that is absorbed by the ocean. As can be seen in Figure 2.12, large regions where less heat is absorbed can be seen in the subtropical gyres in both geoengineering experiments. Of note, there was also more light reflected away near the poles, as sea ice is preserved and augments the ocean's reflectivity. In the tropical South Pacific (east of New Guinea), more light was absorbed due to a loss in cloud cover over this region.

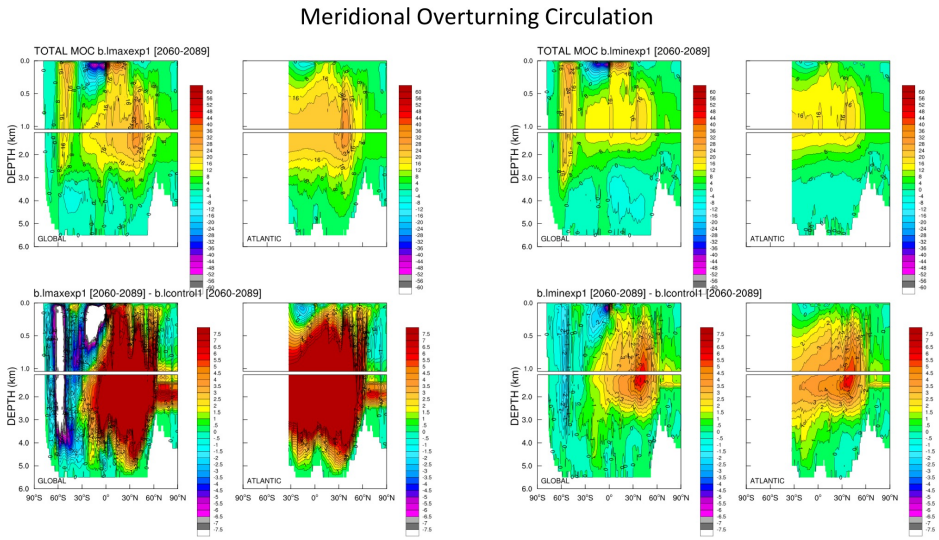

Figure 2.11 The ocean particle geoengineering strategy dramatically accelerates the transport of warm water into the Northwest Atlantic Ocean from the tropics, resulting in the observed warming. Note that the colorbar is saturated within the bottom-left difference panel, and the flow is roughly 3 times greater in the maximal geoengineering experiment relative to the control ($>$ 32 Sv compared to $\approx$ 10 Sv).

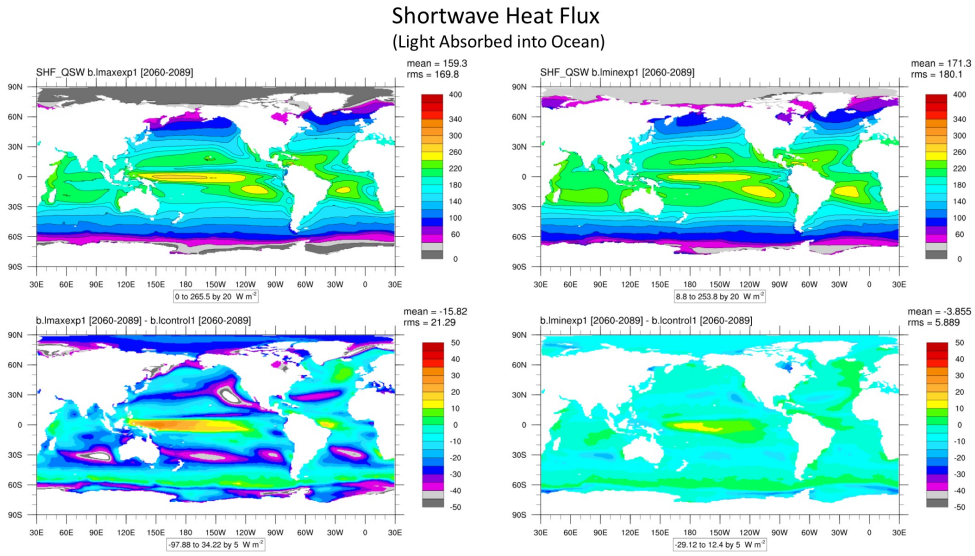

Figure 2.12 Decreased light is absorbed in the subtropical gyres as a direct result of ocean particle geoengineering. Secondary effects include decreased heating near the poles as light is reflected by sea ice, and increased heating in the tropical South Pacific due to a loss of cloud cover.

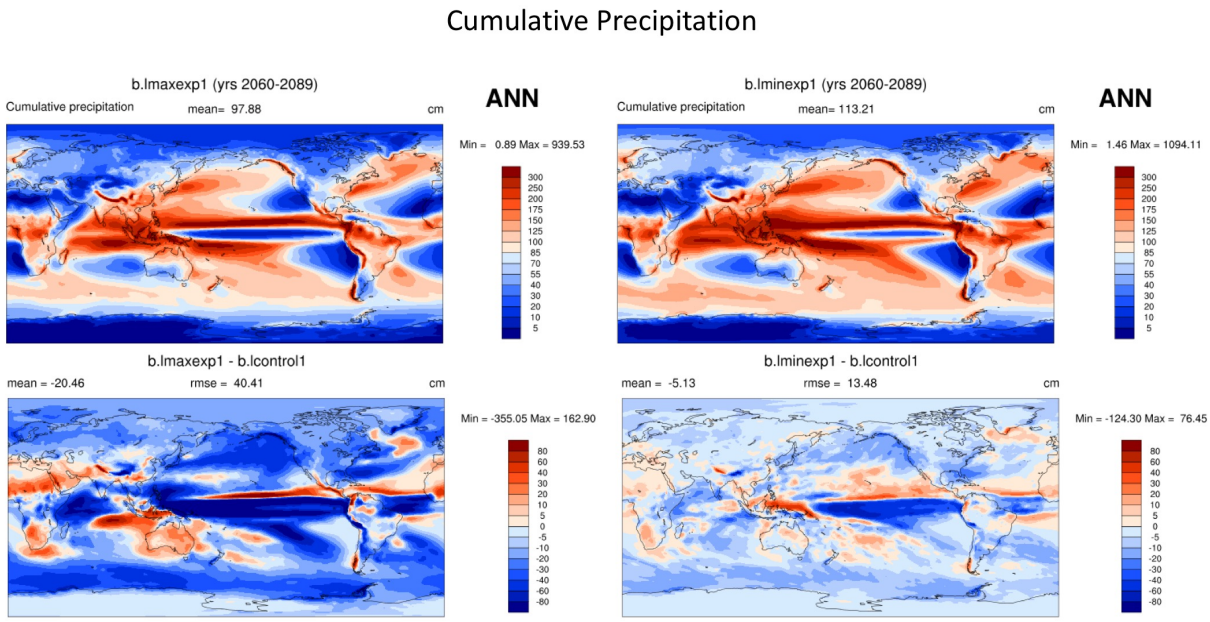

Figure 2.13 The observed precipitation pattern in both geoengineering simulations resembles a La Nina event, in which precipitation decreases in the South-central Pacific. However, there is much greater uncertainty regarding this climate effect, as the regions where precipitation increases are not consistent.

Two other variable fields are of significant interest, but have not yet been examined in great detail. The precipitation pattern observed with both geoengineering cases resembles a La Nina event (see Figure 2.13). Precipitation decreased overall, but this likely reflects a cancellation of the projected average increase in precipitation from climate change (Stocker et al., 2013). Also, the primary ocean productivity (as approximated by the small phytoplankton chlorophyll concentration) was on average decreased by roughly 60% in the maximal geoengineering experiment and increased in the minimal experiment (see Figures 2.14 and 2.15). This decrease was mostly due to light limitation at the poles (where a small fraction of reflective particles were distributed), as primary productivity in the subtropical gyres is usually limited by nutrient scarcity. In November (Figure 2.15) when nutrients are available in these gyres, light scarcity only prevents growth in the maximal case.

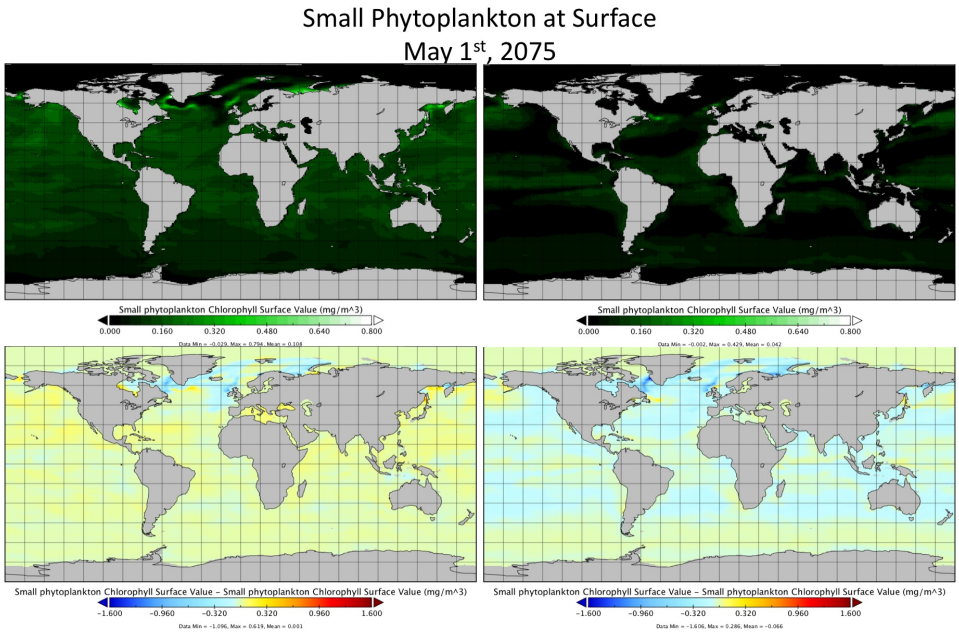

Figure 2.14 The simulated effects of ocean geoengineering on small phytoplankton growth at the surface. Note this figure is a snapshot of one specific date (May 1st) rather than a 30-year average.

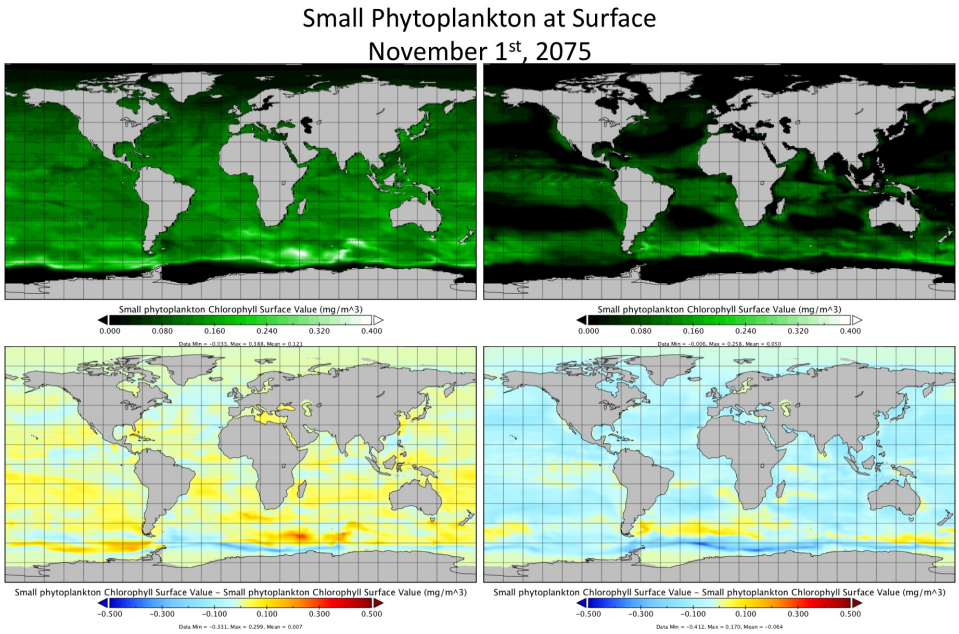

Figure 2.15 The simulated effects of ocean geoengineering on small phytoplankton growth at the surface. Note this figure is a snapshot of one specific date (November 1st) rather than a 30-year average.

Chapter Three

Statistical Filtering

The results of any scientific experiment must be judged within a statistical context (and particularly compared to the null hypothesis), and this usually demands multiple replicates. However, the vast computational resources required to run even a single CESM simulation (with the aforementioned modifications and settings) are vast: upwards of 1700 processor hours per simulated year, or 120,000 processor hours per experimental run. Therefore, I utilized a specialized statistical model, Kalman filtering, to form Bayesian confidence intervals around individual time-series. However, as this technique cannot eliminate bias (should that individual time-series be far from the unknown mean) and assumes a normal distribution, the probabilities I generate cannot be taken as much more than best guesses.

3.1 Kalman Filtering, Smoothing, and Extensions

In the widely used statistical Kalman filtering framework (Kalman, 1960), where subscripts represent time step, let x_n be the variable of interest (an unknown state) at the time step n, and let this variable be affected by three quantities: its prior state x_{n-1}, the time n, and some source of internal noise w_k that is propagated forward to the next time step. This is known as the dynamic equation. At that time, I also make a measurement y_n that reflects x_n but also contains additional measurement noise v_n, the measurement equation. The two

fundamental assumptions of basic Kalman filters are that these functions are linear, and that both sources of noise w_n and v_n have a Gaussian distribution. Linear functions on vectors are matrices, so I can write:

$$\begin{cases} x_n &= \Phi_n x_{n-1} + w_n \\ y_n &= \mathrm{H}_n x_n + v_n \end{cases} \tag{3.1}$$

Likewise, the covariance matrices of these model and measurement errors are respectively:

$$\mathrm{Q} = E[w_n w_n^T] \qquad \mathrm{R} = E[v_n v_n^T] \tag{3.2}$$

Under these assumptions, given all prior and current observations, the optimal estimate of the current state $\overset{*}{x}_n$ and its error covariance matrix $\mathrm{P}_n = E[(x_n - \overset{*}{x}_n)(x_n - \overset{*}{x}_n)^T]$ can be generated inductively, starting with initial estimates for $\overset{*}{x}_0$ and P_0:

$$x_{n|n-1} = \Phi \overset{*}{x}_{n-1} \qquad \text{a priori estimated state projection} \tag{3.3}$$

$$\mathrm{P}_{n|n-1} = \Phi \mathrm{P}_{n-1} \Phi^T + \mathrm{Q} \qquad \text{a priori state covariance projection} \tag{3.4}$$

$$c_n = y_n - \mathrm{H} \overset{*}{x}_{n|n-1} \qquad \text{innovation residual} \tag{3.5}$$

$$\mathrm{S}_n = \mathrm{H}\mathrm{P}_{n|n-1}\mathrm{H}^T + \mathrm{R} \qquad \text{innovation covariance} \tag{3.6}$$

$$\mathrm{K}_n = \mathrm{P}_{n|n-1}\mathrm{H}^T \mathrm{S}_n^{-1} \qquad \text{Kalman gain} \tag{3.7}$$

$$\overset{*}{x}_n = \overset{*}{x}_{n|n-1} + \mathrm{K}_n c_n \qquad \text{a posteriori estimated state} \tag{3.8}$$

$$\mathrm{P}_n = (\mathrm{I} - \mathrm{K}_n \mathrm{H})\mathrm{P}_{n|n-1} \qquad \text{a posteriori state covariance} \tag{3.9}$$

Note that I have dropped the time subscripts on Φ and H in this recursive loop, but they too are updated at each time step. The three new terms introduced above are designated as the innovation covariance S_n, the innovation residual c_n, and the Kalman gain K_n. This past-to-present filter can be extended into a RTS smoother (Rauch, Tung, and Striebel, 1965), which encompasses all known measurements into each estimated state by running

backward from the last known estimates of $\overset{*}{x}_n$ and P_n:

$$\widehat{\mathrm{K}_n} = \mathrm{P}_n \Phi \mathrm{P}_{n|n-1}^{-1} \qquad \text{back-updated Kalman gain} \tag{3.10}$$

$$\widehat{\overset{*}{x}_n} = \overset{*}{x}_n + \widehat{\mathrm{K}_n}(\widehat{\overset{*}{x}_{n+1}} - \Phi \overset{*}{x}_n) \qquad \text{back-updated estimated state} \tag{3.11}$$

$$\widehat{\mathrm{P}_n} = \mathrm{P}_n + \overset{*}{\mathrm{K}}_n(\widehat{\mathrm{P}_{n+1}} - \mathrm{P}_{n|n-1})\widehat{\mathrm{K}_n^T} \qquad \text{back-updated state covariance} \tag{3.12}$$

This Kalman framework can be extended to include a control vector u_n and nonlinear dynamic $F(\cdot, u_n)$ and observation equations $h(\cdot)$:

$$\begin{cases} x_n &= F(x_{n-1}; u_n) + w_n \\ y_n &= h(x_n) + v_n \end{cases} \tag{3.13}$$

The simplest way to achieve this is to linearize $F(\cdot; u_n)$ and $H(\cdot)$ about the previous time step, known as the Extended Kalman Filter (R. E. Kopp and Oxford, 1963; Cox, 1964):

$$\begin{cases} \Phi_n &= \left.\frac{\partial F(x;u_n)}{\partial x}\right|_{x=\overset{*}{x}_{n-1}} \\ \mathrm{H}_n &= \left.\frac{\partial h(x)}{\partial x}\right|_{x=\overset{*}{x}_{n|n-1}} \end{cases} \tag{3.14}$$

More advanced methods exist to ensure that this linearization does not lead the filter astray like the unscented Kalman filter (UKF) (Wan and Van Der Merwe, 2000), but as I will demonstrate later that the EKF is sufficient for these purposes due to the nature of the nonlinear model developed in the following section.

3.2 Weather as a Noisy Climate Signal

Weather reflects the underlying climate with additional stochastic variability arising from dynamic instabilities. For instance, anomalies in mean annual global temperature are primarily due to El Nino events in the tropical Pacific, which typically oscillate with a period of less than 5 years (Hu and Fedorov, 2017). It is a common convention ((WMO), 2017) to report the climate as the 30-year running average of temperature ($_{30} < T >$).

Therefore, in order to make a probabilistic estimate of the effects of climate interventions in real time, I propose the weather system fits into the Kalman filtering framework:

$$\begin{cases} {}_{30}< T >_n & = F({}_{30}< T >_{n-1}, u_n) + w_n \\ T_n & = {}_{30}< T >_n + v_n \end{cases} \tag{3.15}$$

Utilizing the HadCRUT4 dataset because it extends back to 1850 (which is also the start point for 20th century runs within CMIPs), I can generate estimates of the measurement covariance matrix R. For instance, if I take T_n to be a one-dimensional mean temperature of the whole planet, then I generate the following graph: The standard deviation of the

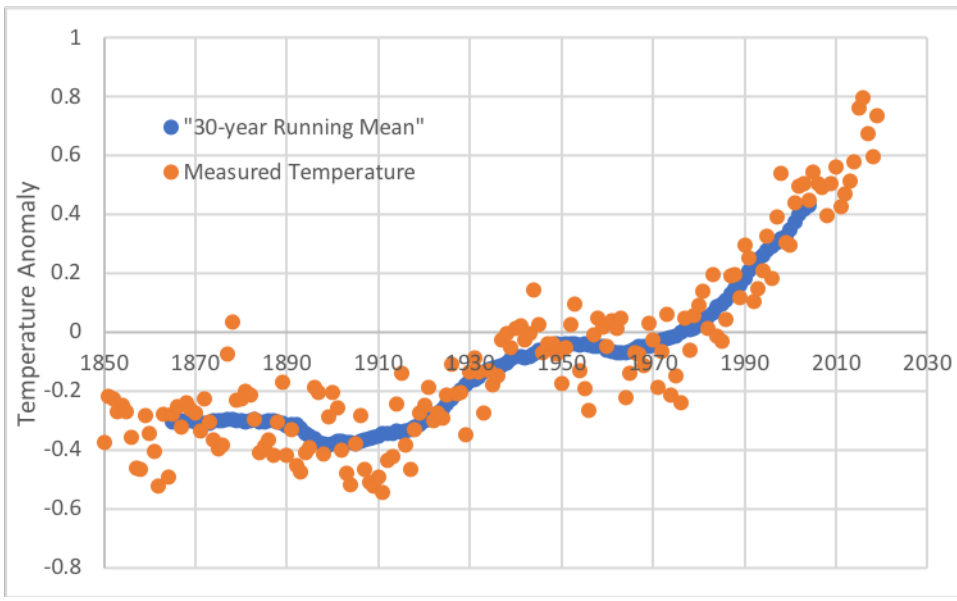

Figure 3.1 Temperature anomaly from HadCRUT4 (Morice et al., 2012) compared to the 30-year running mean

difference between the 30-year running mean and the yearly temperature is 0.103. This distribution is very close to being Gaussian, so a portion of the Kalman filtering assumptions are met.

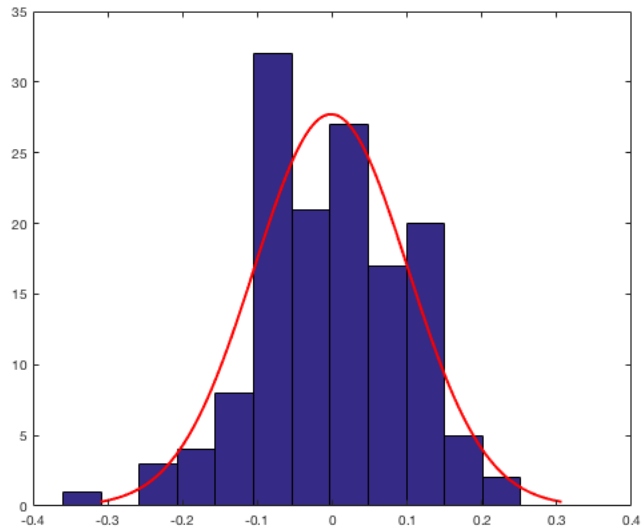

Figure 3.2 Histogram of differences between annual temperature anomaly and 30-year running mean, with normal distribution overlaid in red. Standard deviation is 0.103. This does not form a perfect normal distribution, but it is close enough for the Kalman filter to make a good approximation.

3.2.1 Derivation of Dynamic Equation

I begin by examining a toy model involving a uniform planet and the principal energy fluxes. This model was inspired by the work of other published energy-budget models (Hu and Fedorov, 2017; Kravitz, Rasch, et al., 2018).

$$E_{flux} = SW_{in} \qquad -LW_{out} \tag{3.16}$$

$$\frac{T_n - T_{n-1}}{k} C_{heat} = (Sol_{rad}(absorption)) \qquad -(\sigma_{sf}(T_{n-1})^4(1 - backscatter)) \tag{3.17}$$

k is 1 year, the time step of this model. T^4 is the ideal black body radiation, which derives from quantum mechanics, particularly the Stefan–Boltzmann law (Boltzmann, 1884), from which I get the Stefan-Boltzman constant $\sigma_{sf} = 5.670 * 10^{-8} W m^{-2} K^{-4}$. For the Earth, because the temperature is in the neighborhood of 287K, this black body radiation is primarily in the infrared spectrum, between the range of 200 and 1200 cm^{-1} (Zhong and Haigh, 2013). While a portion of this light β_0 back-scatters off of the atmosphere due to

gasses other than CO_2, the back-scattering from CO_2 is directly proportional by β_1 to the logarithm of the CO_2 concentration (see Figure 3.3).

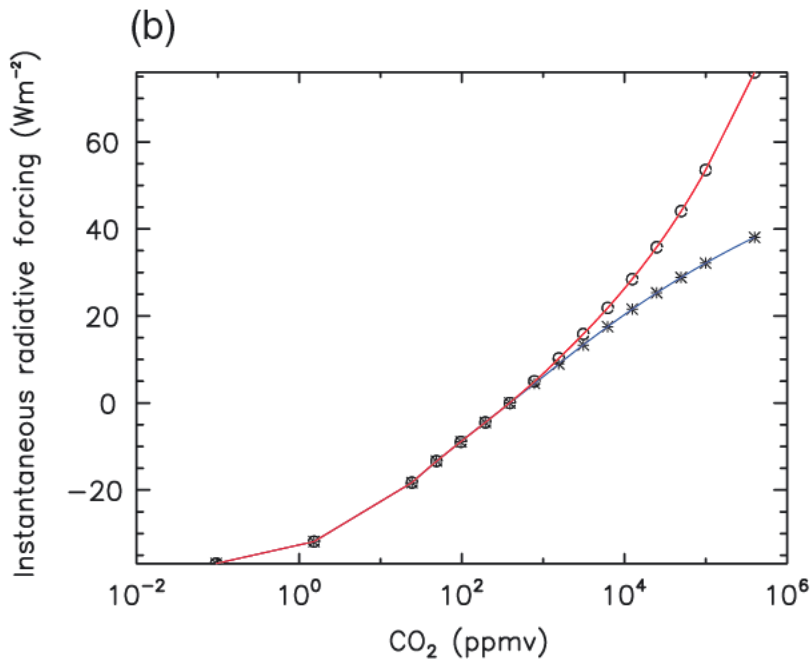

Figure 3.3 Linear correlation between $\log[CO_2]$ and the proportion of LW_{out} that is back-scattered. Adapted from (Zhong and Haigh, 2013). The red line represents the back-scattering due to CO2 at all infrared frequencies, whereas the blue line is just the spectral region 550-800 cm^{-1}

$$E_{backscatter} = E_{greenhouse-absorb}/2 \approx \Big(\beta_0 + \beta_1 \log_{10}([CO_2])\Big) E_{total} \tag{3.18}$$

The rationale behind this correlation can be demonstrated by a series of simplifications, particularly Beers Law and approximating absorption peaks as normal distributions. Of the outgoing radiation that is absorbed by greenhouse gases ($E_{greenhouse-absorb}$), principally carbon dioxide and atmospheric water, half is re-emitted outward by this layer, and half is back-scattered back to the surface. See Appendix C1 for a more detailed explanation.

The overall albedo of Earth is primarily determined by clouds and the optical properties of the dominant surface in each biome, which change relatively little on an annual basis

(Stephens et al., 2015). Reductions in sea ice and snow cover may be traded for increases in clouds, such that no global albedo change is yet attributable to anthropogenic climate change (Loeb, Lyman, et al., 2012), although the Arctic albedo has decreased dramatically (Pistone, Eisenman, and Ramanathan, 2014). Therefore, I assume an underlying albedo of $\beta_2 = albedo_{const} = 0.29$, as measured by the CERES satellite (Wielicki et al., 1996; Loeb, Wielicki, et al., 2007).

On a year-to-year basis, I assume that anomalies in the planet's albedo are primarily determined by atmospheric aerosols generated by volcanic eruptions. Unlike carbon dioxide absorption, the light reflected by these aerosols is broad spectrum (hence clouds of dust appear white). Therefore, I translate the aerosol optical depth reported by (Sato et al., 1993; Vernier et al., 2011) into units of energy:

$$\tau = \log(\frac{E_{rec'd}}{E_{trans'd}}) \tag{3.19}$$

$$e^{-\tau} = \frac{E_{trans'd}}{E_{rec'd}} \tag{3.20}$$

To translate this into units of albedo, let's approximate that of the light which is not transmitted through the atmosphere, all the energy of the light not absorbed by the top layer of the atmosphere is reflected directly back into space, whereas the rest is absorbed. Again by Beer's Law, if that top atmosphere layer is proportion β_3 of the total, then

$$\beta_3\tau = \log(\frac{E_{rec'd}}{E_{trans'd}}) \tag{3.21}$$

$$e^{-\beta_3\tau} = 1 - \frac{E_{refl'd}}{E_{rec'd}} \tag{3.22}$$

$$1 - e^{-\beta_3\tau} = \frac{E_{refl'd}}{E_{rec'd}} = albedo_{aerosols} \tag{3.23}$$

Since this now considers two kinds of albedo, the fractions of light which are not reflected

at each level (top of atmosphere and surface) are multiplied together as below:

$$\begin{aligned} absorption =& (1 - albedo_{const})(1 - albedo_{aerosols}) && (3.24)\\ =& (1 - \beta_2)\big(1 - (1 - e^{-\beta_3 \tau})\big) && (3.25)\\ =& (1 - \beta_2)e^{-\beta_3 \tau} && (3.26) \end{aligned}$$

While the annual total solar irradiance Sol_{rad} does vary by 0.1% between solar minima and solar maxima on a cycle lasting about 11 years (G. Kopp and Judith L. Lean, 2011; Wang, J. L. Lean, and Sheeley, 2005; Willson and Hudson, 1991), for the purposes of the this toy model I assumed a constant 1364 W/m^2, or 341 W of insolation per m^2 of Earth's surface area. In a later version of the model, this constant parameter was allowed to be tuned to values in the neighborhood of 341 W/m^2. Assuming this value, in a steady-state climate equilibrium with no volcanic eruptions, 242 W/m^2 of shortwave light is absorbed by the climate system.

Figure 3.3 from (Zhong and Haigh, 2013) tells us that for every order of magnitude by which $[CO_2]$ increases, an additional 15.45 W/m^2 is absorbed. This assumes a constant black body temperature, which I will assume to be 286K in a steady-state climate equilibrium. This allows us to solve for β_0 and β_1 as follows, with the additional information that in the pre-industrial climate, $log_{10}([CO_2]) \approx 2.45$:

$$\begin{aligned} \frac{T_n - T_{n-1}}{k} C_{heat} = 0 &= (Sol_{rad}(absorption)) - (\sigma_{sf}(T_n)^4(1 - backscatter)) && (3.27)\\ 0 &= 341W/m^2(0.71) - \sigma_{sf}(T_n)^4(1 - \beta_0 - \beta_1 \log_{10}([CO_2])) && (3.28)\\ 242W/m^2 &= \sigma_{sf}(286K)^4(1 - \beta_0 - \beta_1(2.45)) && (3.29)\\ 15.45W/m^2 &= \sigma_{sf}(286K)^4(\beta_1) && (3.30)\\ 0.0407 &= \beta_1 && (3.31)\\ 0.633 &= 1 - \beta_0 - 0.0407(2.45) && (3.32)\\ 0.267 &= \beta_0 && (3.33) \end{aligned}$$

Finally, the value of C_{heat}, representing the heat capacity of the whole climate system and land mass on a yearly time scale, was a quantity that involved substantial uncertainty. Reported literature values of this heat capacity are 17 ± 7 W (year) m^{-2} K^{-1}, (Schwartz, 2007).

Combining all of these derivations and notating the values which change at time n (but eliminating units for simplicity), I obtain the following as the dynamic equation

$$\frac{T_n - T_{n-1}}{k} C_{heat} = SW_{in}(1-\beta_2)e^{-\beta_3 \tau_n} \quad -(\sigma_{sb}(T_{n-1})^4(1-\beta_0-\beta_1 \log_{10}([CO_2]_n))) \tag{3.34}$$

$$T_n = \frac{SW_{in}k}{C_{heat}}(1-\beta_2)e^{-\beta_3\tau_n} \quad +T_{n-1}\big(1-\frac{\sigma_{sb}k}{C_{heat}}T_{n-1}^3(1-\beta_0-\beta_1\log_{10}([CO_2]_n))\big) \tag{3.35}$$

$$T_n = \alpha_1(\tau_n) \quad +T_{n-1}\big(1-\alpha_2([CO_2]_n) \quad T_{n-1}^3\big) \tag{3.36}$$

$$T_n = F(T_{n-1}; \tau_n, [CO_2]_n) \tag{3.37}$$

This dynamic equation was first run as a blind model, merely running the dynamic equation recursively without changing any parameters or state variables based on observations. The trajectory of this blind model was then compared to the 30-year mean, shown as black in Figure 3.4 in order to tune the parameters. The blind model was initialized with a temperature of 286.7K as this was the starting temperature of the 30-year mean (see Figure 3.4). In yellow, parameter values were taken as derived from literature sources above (with $\beta_3 = 0$). However, this yellow blind model substantially underestimated the sensitivity of the climate system to CO_2. Thus, the blind model was fit to the 30-year mean using sum of squared differences minimization with Microsoft Excel's GRG nonlinear optimization, varying only the parameters $C_{heat}, \beta_0, \beta_1$ and β_3 to keep the model identifiable. This modified blind model is displayed in magenta, and the updated parameters are displayed in the inset table. Note that β_1 increased by more than 75% and β_2 decreased to compensate, while C_{heat} increased from 17 to 43. In orange, there is an intermediate blind model in which $\beta_3 = 0$ but the other parameters ($C_{heat}, \beta_0, \beta_1$) are fit, and these take similar values as the purple blind model.

Blind Model Description	R^2	C_{heat}	β_3	β_1	β_0
Literature Parameter Values	0.7005	17	0	0.0407	0.2674
Fitted Param. Values w/o β_3	0.9366	43.41	0	0.0715	0.1914
Fitted Param. Values including β_3	0.9531	42.89	0.0533	0.0722	0.1904

Table 3.1 Values of fitted coefficients in blind model

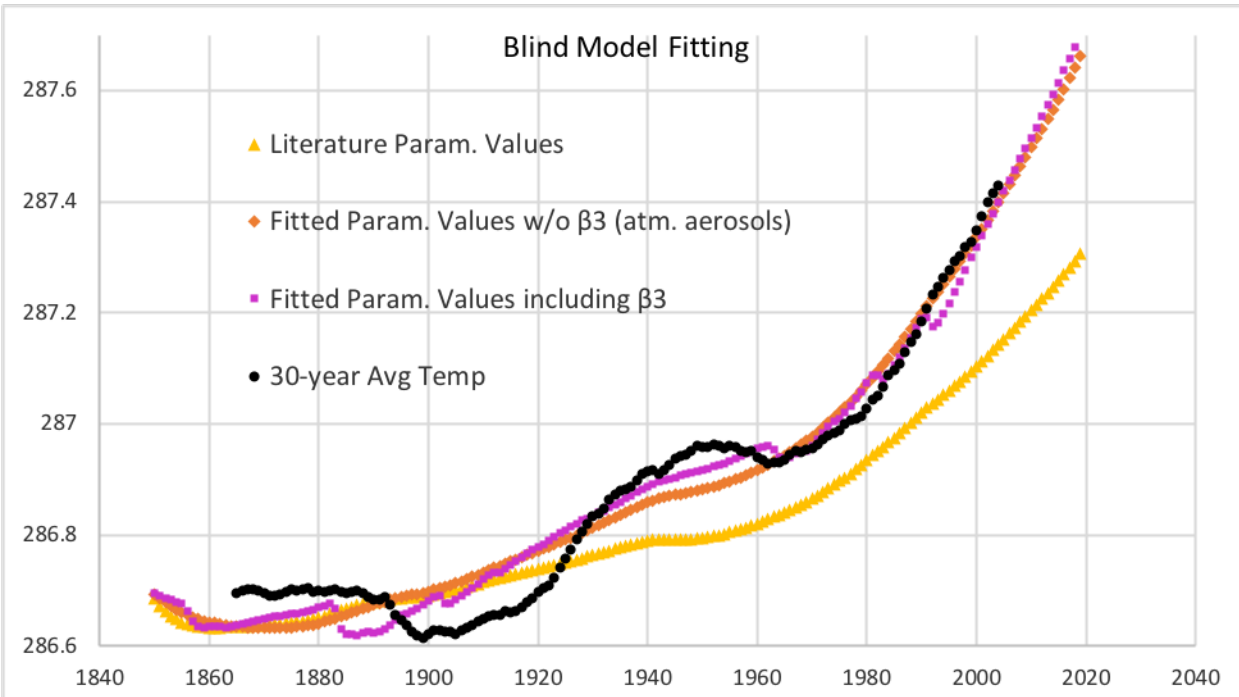

Figure 3.4 Comparison of the various blind models to the 30-year running mean of the HadCRUT temperature. Discussion of this figure is in the preceding paragraph. Parameter values are listed in Table 3.1.

3.2.2 Completion of EKF

Returning to the functional form of F in Eq. 3.36, note that this is a non-linear function. It includes both a time-varying term $\alpha_{1,n}$ and a fourth power of T_{n-1}, with a time-varying coefficient $-\alpha_{2,n}$. (Note that all of the time-varying control parameters and fitted β's have been absorbed into these two time-varying parameters of the fundamental model, and I

sometimes notate α_1 and α_2 with their critical control parameters in parentheses.)

$$\alpha_1(\tau_n) = \frac{SW_{in}k}{C_{heat}}(1-\beta_2)e^{-\beta_3\tau_n} \qquad = \alpha_{1,n} \tag{3.38}$$

$$\alpha_2([CO_2]_n) = \frac{\sigma_{sb}k}{C_{heat}}(1-\beta_0-\beta_1\log_{10}([CO_2]_n)) \qquad = \alpha_{2,n} \tag{3.39}$$

The projection step of the Kalman filter requires that I somehow include both of these nonlinear terms. So, the extended Kalman filter (EKF) simply requires the derivative of this function F with respect to T_{n-1} at time n.

$$\Phi_n = \frac{\partial F(T_{n-1};\tau_n,[CO_2]_n)}{\partial T_{n-1}} = \big(1-4T_{n-1}^3\alpha_2([CO_2]_n)\big) \tag{3.40}$$

However, the basic Kalman filter update equation 3.3 no longer holds, as merely taking $\Phi_n T_{n-1}$ does not resemble the original function F. Therefore, I will merely replace the projection equation 3.3 with the real definition of F:

$$\overset{*}{T}_{n|n-1} = \alpha_1(\tau_n) + \overset{*}{T}_{n-1}\big(1-\alpha_2([CO_2]_n)(\overset{*}{T}_{n-1})^3\big) \tag{3.41}$$

Also rewriting equation 3.11 for the RTS smoother, this function F again replaces $\Phi_n T_{n-1}$

$$\overset{**}{T}_n = \overset{*}{T}_n + \overset{*}{\mathrm{K}}_n\left(\overset{**}{T}_{n+1} - \alpha_1(\tau_n) - \overset{*}{T}_n\big(1-\alpha_2([CO_2]_n)(\overset{*}{T}_n)^3\big)\right) \tag{3.42}$$

which backward-propagates the information from new measurements to the smoothed ideal climate temperature in the past. In the course of running this RTS Smoother, I found that the results only differ slightly from the EKF. Therefore, the primary focus of this thesis will remain on the EKF, which incorporates information only up to the current time point. However, comparisons are most appropriate between the 30-year running mean temperature and the model state of this RTS Smoother, as both metrics incorporate information from both the past and future.

Justification that EKF will not diverge

The time-dependent values of α_1 and α_2 do not vary dramatically: $\alpha_1 = 5.637 \pm 0.006$ and $\alpha_2 = 8.310 \pm 0.040 * 10^{-10}$. Therefore, there is a very strong negative feedback arising from the

$-T^4$ term, which will keep any Kalman filter predictions (particularly those from an UKF) locked into the region immediately surrounding the blind model prediction. The amount by which the true hidden climate temperature changes, $T_n - T_{n-1} = F(T_{n-1}; \tau_n, [CO_2]_n) - T_{n-1}$, looks quite linear in the vicinity of 287.6K. Therefore, I do not have to worry about filter divergence, and the EKF is more than sufficient for this purpose of planetary average climate modeling.

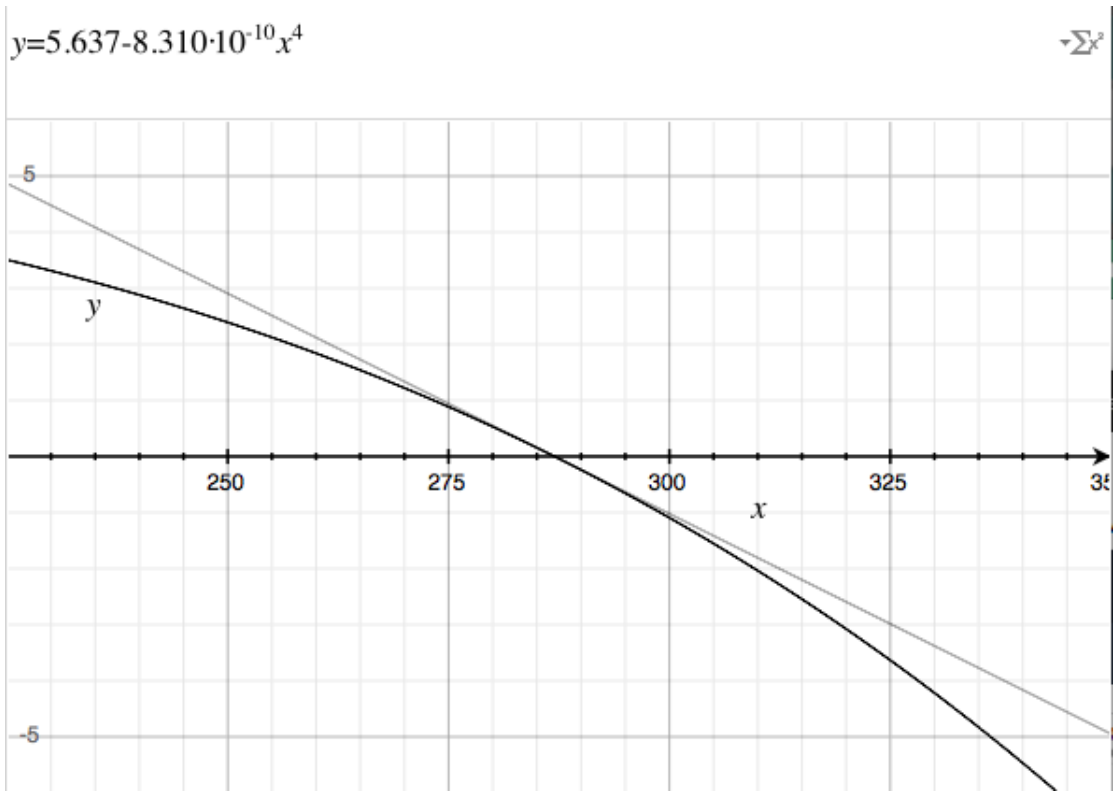

Figure 3.5 Graph of the update equation, the amount by which T will change over the next time step gives its current value and a constant α_1 and α_2. Note that this only has one intercept (one stationary point), and there is a good linear fit in this region.

3.3 Initial Results on Historical Data

The blind-model-fitted β values (including β_3 were plugged into an EKF with the "noisy measurements" of yearly temperature coming from the aforementioned HadCRUT dataset. The values of the model and measurement error were adjusted individually to $Q = 0.001, R = 0.007$, and the results look very promising. In particular, Figure 3.6 shows the 5 ways of analyzing the global temperature from 1850 through 2019: plotting raw, averaging, predicting, filtering, and smoothing. All of these lines and scatters show a very similar overall trend, with temperature remaining nearly constant until 1925, rising by about 0.3K, then briefly plateauing between 1950 and 1975, only to resume warming at a rate of 0.9K per 50 years. Furthermore, the Kalman filter (and smoothed) climate states appear to more closely match the 30-year averaged climate temperature than either the raw temperature or the blind model prediction.

Next, the innovation (co)variance S_n and the EKF a priori estimated state are compared to "noisy" yearly measurements of temperature $y_n = T_n$ in Figure 3.7. I write (co)variance because this term is currently a scalar rather than a matrix. Notice in the figure that the initial large estimate of this variance (due to a large initial guess of P_0) is rapidly burned off. Assuming that the Kalman filter estimated state closely approximates the true "climate state" then these innovation residuals should be normally distributed. In Figure 3.8, observe that the distribution is indeed very close to normal. Furthermore, S_n is the most appropriate value to use to make this comparison, as it combines time-varying uncertainty regarding the model state and the constant "measurement error" R, and thus allows for the generation of a marginal likelihood of the observations.

$$\log(P[y_{0..169}]) = \log \prod_{n=0}^{169} \mathcal{N}\left(y_n; H_k \overset{*}{x}_{n|n-1}, S_k\right) \tag{3.43}$$

$$= \sum_{n=0}^{169} -\frac{1}{2}\left(c_n^{\mathsf{T}} S_n^{-1} c_n + \log|S_n| + (1)\log 2\pi\right) \tag{3.44}$$

(There are 169 years from 1850 to 2019, and the (1) is due to the fact that the observations

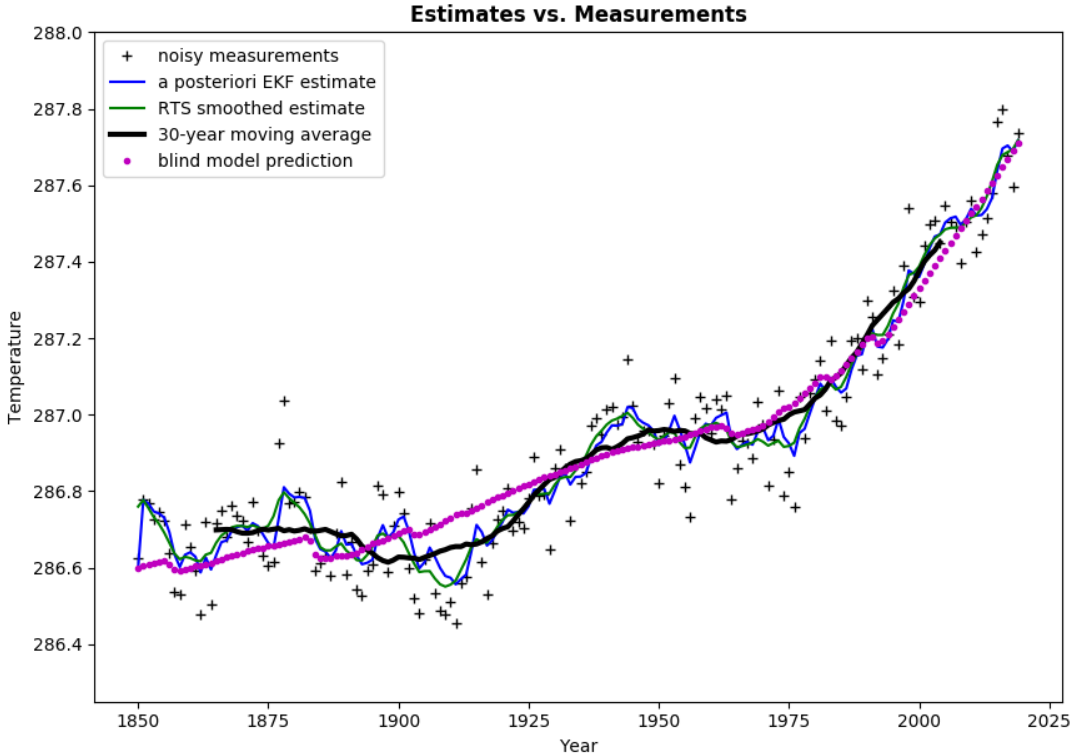

Figure 3.6 The blind model (again in magenta) and the 30-year running mean temperature (again in black) are now joined by the EKF $\overset{*}{x}_n$ and RTS $\widehat{\overset{*}{x}_n}$ forward posterior estimates in blue and green. Annual measurements of temperature are shown in +, which direct the EKF and RTS estimates of the true climate state. Note that the EKF and RTS estimates are usually in between the 30-year mean temperature and any bumps in annual temperature, such as the cooler years that occurred around 1910.

are one-dimensional). $\sqrt{S_n} = \sigma$ consistently has a value of $\pm 0.098K$, meaning that about 73% of the innovation (co)variance arises from the prescribed measurement uncertainty R.

Next, the RTS backward-updated estimates of the model state and state (co)variance are compared to the 30-year average temperature measurements (see Figure 3.9). Here, the $_{30} < T >_n$ is taken to be the truth value of the x_n that I am trying to estimate. This is a bit of a stretch, but I want to ensure that the Kalman estimates behave as closely as possible to an consensus-recognized measurement of the "climate state". Note that the final

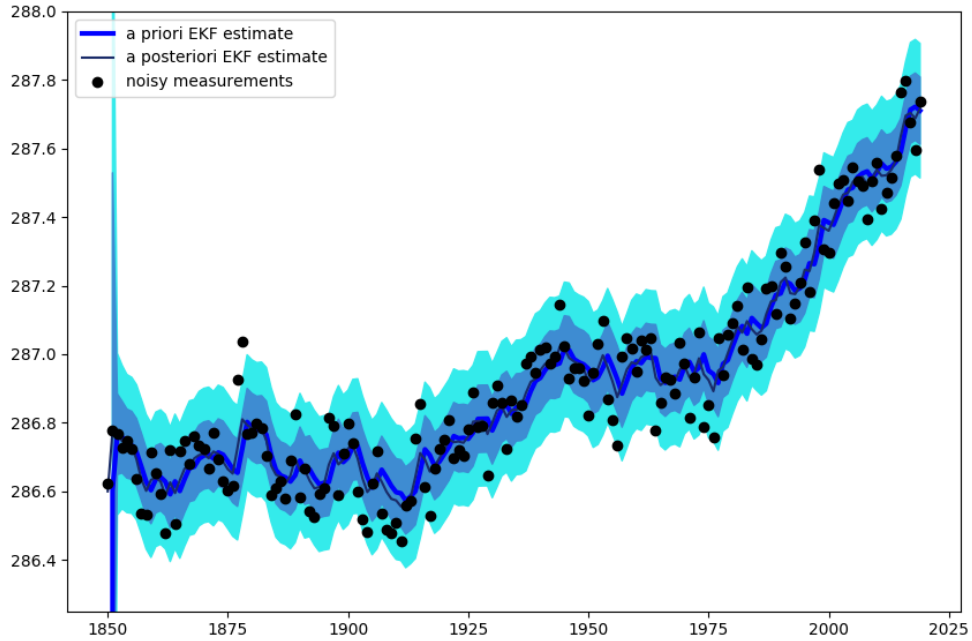

Figure 3.7 EKF forward posterior $\overset{*}{x}_n$, with 1σ and 2σ windows of the innovation (co)variance $\sqrt{S_n}$, compared to the annual measurements of temperature.

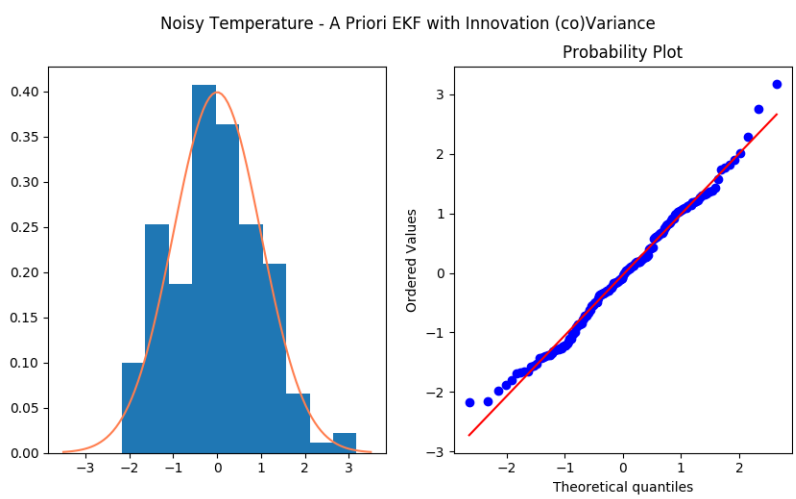

Figure 3.8 The EKF innovation residuals c_n are fit nicely to a normal curve, so they are nicely predicting the distribution of temperature measurements.

uncertainty in the model state $\widehat{\mathrm{P}_n}$ is significantly less than the innovation uncertainty S_n. In particular, $\sigma = \sqrt{\widehat{\mathrm{P}_n}} \approx \pm 0.036K$. Surprisingly, these 30-year averages also appear to be normally distributed about the RTS state estimate (adjusting for the state uncertainty), as can be seen in Figure 3.10. Similarly to before, the marginal likelihood of these model states are calculated as follows. (Note that there are fewer years in the series, because the 30-year moving average requires a 15-year buffer before and after $x_n =_{30} < T >_n$.)

$$\log(P[x_{15..154}]) = \log \prod_{n=15}^{154} \mathcal{N}\left(x_n; \widehat{\overset{*}{x}_n}, \right) \tag{3.45}$$

$$= \sum_{n=15}^{154} -\frac{1}{2}\left((x_n - \widehat{\overset{*}{x}_n})^{\mathsf{T}} \widehat{\mathrm{P}_n}^{-1} (x_n - \widehat{\overset{*}{x}_n}) + \log \left|\widehat{\mathrm{P}_n}\right| + (1)\log 2\pi \right) \tag{3.46}$$

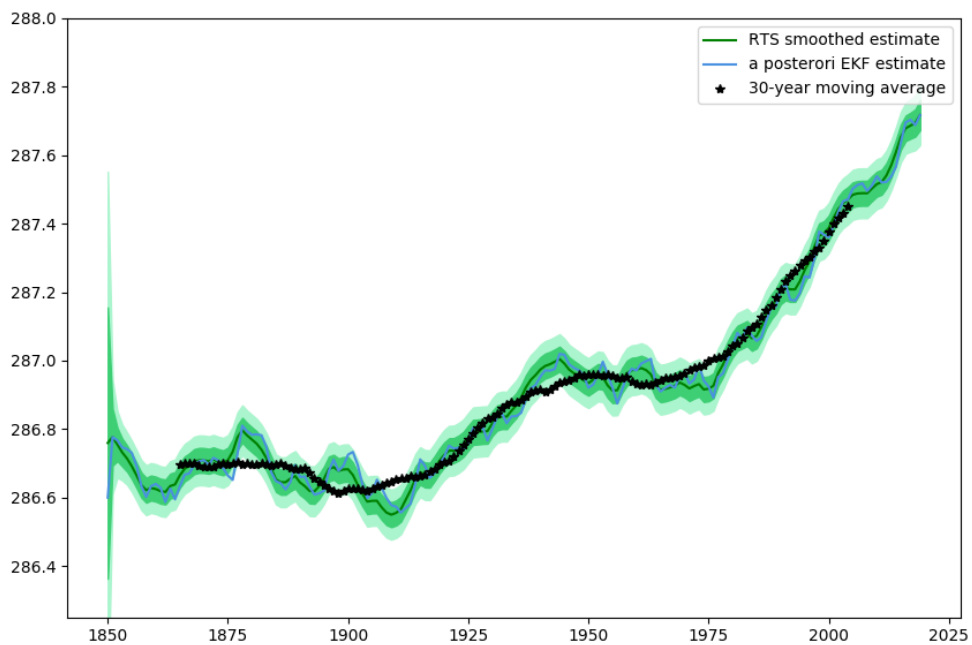

Figure 3.9 RTS-smoothed estimate $\widehat{\overset{*}{x}_n}$, with 1σ and 2σ windows of the backward-updated state covariance, compared to the 30-year average of temperature (black stars). The a posteriori EKF estimate $\overset{*}{x}_n$ is also plotted on this figure in blue.

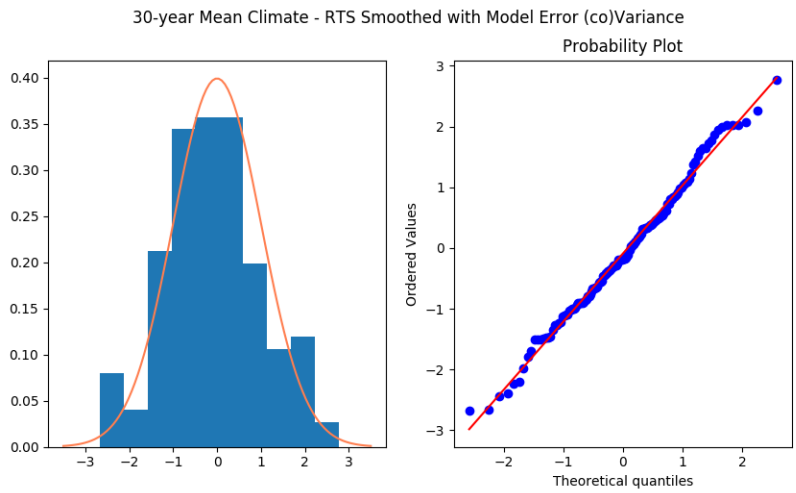

Figure 3.10 The distribution of differences between the RTS-estimated state $\widehat{x_n^*}$ and $_{30} < T >$, adjusted for the RTS-estimated state covariance. This normal distribution implies that the RTS state and state (co)variance are fit nicely to predict the 30-year mean temperature measurements.

3.3.1 MCMC Variation of Parameters

To ensure that there was not a better combination of the time-invariant parameters of the Kalman filter model, I conducted a Metropolis-Hastings search of the parameter space. To prevent issues with generating non-identifiable models, I only included the parameters $C_{heat}, \beta_0, \beta_1, \beta_3, R$ and Q. Each of these parameters was varied by simultaneously sampling in a multivariate normal distribution about these parameters' current value, with standard deviations proportional to these parameters initial values (from the blind model fitting). The total log-likelihood of each sample was computed as the sum of the log-likelihoods of the 30-year averaged climate $\log(P[x_{15...154}])$ and the "noisy" annual temperatures $\log(P[y_{0...169}])$. This was then multiplied by an adjustment factor of 1/10 to reflect the average log-likelihood of a collection of 31 individual temperature or climate measurements. This reduced the absolute probability difference between sampled parameter values and encouraged the Metropolis-Hastings algorithm to explore the parameter space (see Figure 3.11).

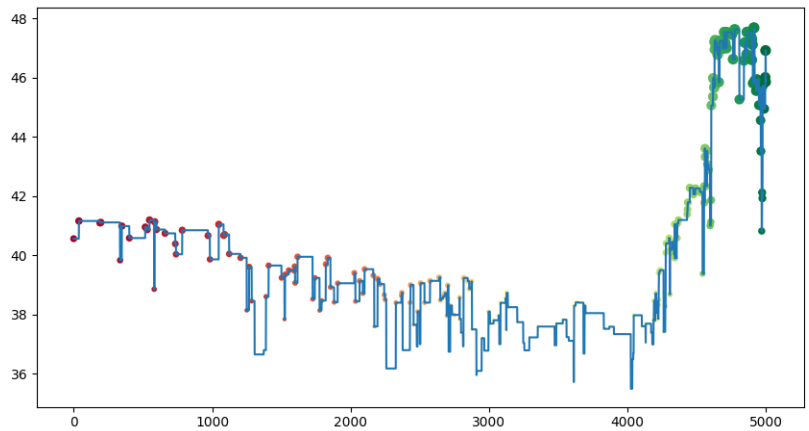

Figure 3.11 The adjusted log-likelihood score evolution over time in the MCMC model over the course of 5000 trials. Dot size corresponds to the adjusted log-likelihood of the accepted sets of parameter values. The color of these dots corresponds to the order with which these accepted parameter values appeared, with red corresponding to early in the run (burn-in period) and green corresponding to later.

The average probability density (likelihood) at a single measurement (either of $T_n = y_n$ or $_{30} < T >_n = x_n$) is roughly 1.3 throughout this MCMC run. Rather than using a principal component analysis to display the changes within the specified 6 parameters (which would obscure their physical meaning), they are plotted in Figure 3.12 in pairs corresponding to those which were most strongly correlated (see 3.2). Furthermore, the figures displaying this Metropolis-Hastings simulation do not include an earlier burn-in period of approximately 1000 trials which only changed the blind-fitted parameter values by ±20%. The small orange points sweep back very near to the blind-fitted parameter values.

Unfortunately, the converged results from this Metropolis-Hastings search with the greatest log-likelihood are also physically unrealistic. As can be seen in the upper-right panel of Figure 3.12, in the later green samples C_{heat} grew to a very large size, all >500. Recalling the original literature value of 17 ± 7 W (year) m^{-2} K^{-1}, (Schwartz, 2007) and judging these values to be far too high, $1/C_{heat}$ was plotted rather than C_{heat}. This allowed

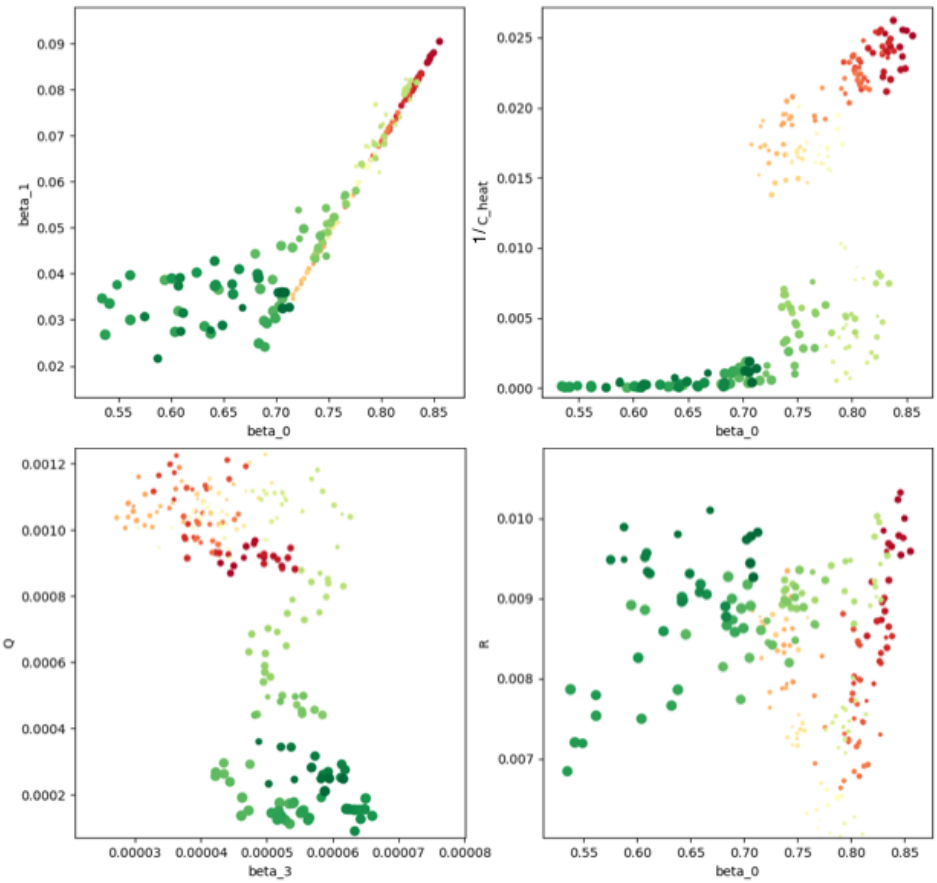

Figure 3.12 The parameters $1/C_{heat}, \beta_0, \beta_1\beta_0, \beta_3, Q$, and R evolving over the course of the Metropolis-Hastings search. The point size corresponds to the log-likelihood. Red points represent the burn-in phase, whereas green colors represent points that are sampled later.

the earlier values to not be compressed near 0. In one accepted sample (with a high adjusted log-likelihood), the value of C_{heat} exceeded 25000 W (year) m^{-2} K^{-1}. A heat capacity per square meter this high would correspond to a column of water 200km deep.

$$\frac{2.5 * 10^4 W(year) m^{-2} K^{-1} * 3.154 * 10^7 \frac{s}{year}}{4.184 J g^{-1} K^{-1} * 10^6 \frac{g}{m^3} \text{ for water}} \approx 2 * 10^5 m \tag{3.47}$$

Therefore, this use of Metropolis-Hastings sampling did not allow us to discover the uncertainty regarding the unknown parameter values, as intended. This failing occurred because the parameter which was least known in the earlier blind model, C_{heat}, exploded in magnitude to a ridiculously large size. I could re-adjust the summed log-likelihood

C_{heat}	β_3	β_1	β_0	Q	R
1.	0.6358	0.5507	-0.7094	0.7435	-0.2512
0.6358	1.	0.8845	-0.3169	0.7373	-0.1259
0.5507	0.8845	1.	-0.1123	0.5988	-0.0890
-0.7094	-0.3169	-0.1123	1.	-0.6114	0.4274
0.7435	0.7373	0.5988	-0.6114	1.	-0.4039
-0.2512	-0.1259	-0.0890	0.4274	-0.4039	1.

Table 3.2 Correlations between MCMC-sampled parameters. The very strong negative correlation between β_0 and β_1 is likely real because of Eq 3.29-3.33. However, many other correlations may largely reflect the shift to the modes in which C_{heat} is unrealistically large.

computation or the sampling distributions to discourage such high estimates of C_{heat}, but such efforts are beyond the scope of this thesis. The original blind-model parameter values are sufficient.

3.3.2 Comparison with CESM LENS Ensemble

A very different approach for generating uncertainty regarding the state of the climate system involves ensembles of climate model hind-cast runs. These runs utilize historical concentrations of carbon dioxide and atmospheric aerosols from volcanic eruptions, but start the numerical model at different initial conditions. Parameters within these physical simulations are tuned to reflect climate observations, just as the various parameters were tuned within the blind model. Analogous to the fundamental assumption for the Kalman filter that the climate system is Gaussian noise atop a dynamic equation that also includes noise, assumptions are made within climate models for the physics equations that determine the model's behavior (as fractal features like mesoscale eddies must be paramaterized).

Due to the chaotic yet bounded nature of the climate system, this ensemble quickly loses any predictable artifacts of the differing initialization and samples the entirety of the state-space within the climate model. Therefore, I attempted a comparison between the Kalman filter and the 41 CESM LENS runs of the 20th century (Kay et al., 2015). The

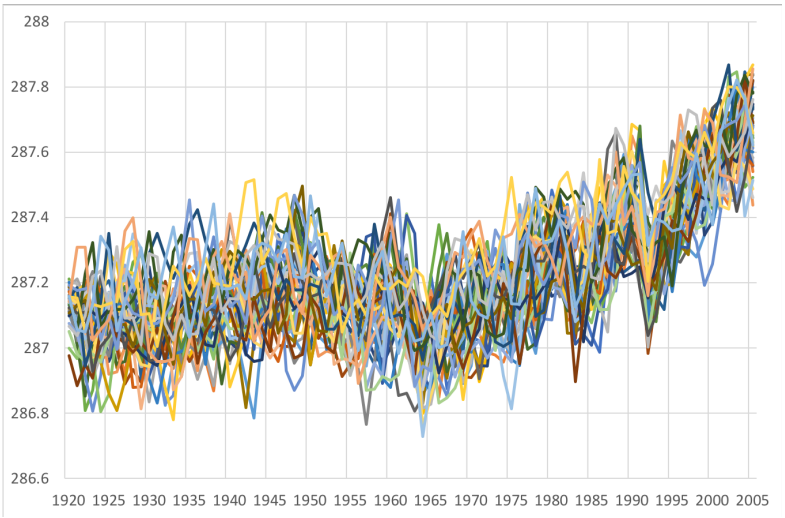

Figure 3.13 The LENS hind-cast simulation over the years 1920-2006. Note that colors are chosen at random to allow the reader to follow the 41 individual simulation runs.

results from these runs, particularly regarding globally averaged surface temperature, are shown in Figure 3.13.

Thus, at each year I have 41 samples of the temperature, which can be used to generate a distribution. This distribution generally looked normal, and had a fairly consistent standard deviation of 0.11 ± 0.01. Therefore, I compared the prediction distributions of temperature generated by both the Kalman filter and this LENS ensemble in Figure 3.14.

Recall that the original HadCRUT data was presented as temperature anomalies and then shifted up by (chosen arbitrarily) 287K to get absolute temperature. The Kalman filter was also based on the assumption of a steady-state pre-industrial climate that determines β_0 and β_1 (see Eq. 3.29-3.33), so these parameters reflected the (arbituarily shifted) temperature data. Furthermore, it is common practice in climate model inter-comparison projects to shift the results so they match in the average temperature and analyze only the trend (Masson-Delmotte et al., 2018). So it is reasonable for several reasons to perform the vertical shift in temperature (as noted in 3.14) to compare these two predictive models.

Regarding quantitative measurements to compare these two time-series of distributions,

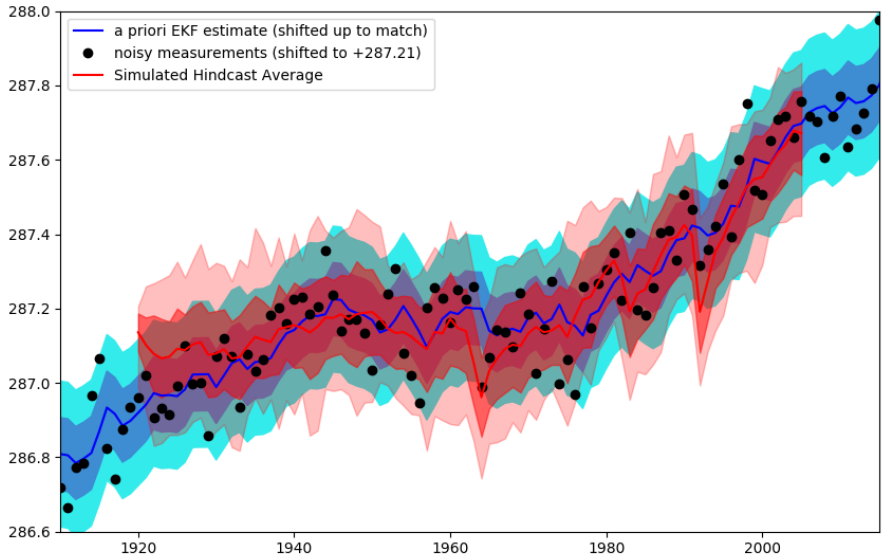

Figure 3.14 The LENS hind-cast simulation in red compared to the Kalman filter prediction of the next year's temperature in blue, with 1σ and 2σ of uncertainty. Temperature data and Kalman fiter are shifted to a higher temperature by roughly 0.2K. Note that while I am using the standard calculation of standard deviation for the LENS 1σ confidence interval, to reflect the fact that this distribution may not truly be normal, the 2σ confidence interval is between the midpoints of the two largest and the two smallest values ($\frac{39}{41} \approx 0.95$).

I tried to apply the Anderson-Darling test smeared over all time points, but this yielded a very significant difference ($p \approx 10^{22}$). I suspect that the formula may need to be revised for it to be applied in this manner, or perhaps separate tests could be performed on the trend in distribution means (R^2) and the variances (an F test). Regardless, in qualitative terms, the two distributions follow a very similar shape (roughly piece-wise linear with a rise before 1940, then constant until 1975, then a more rapid increase, as described previously in reference to Figure 3.6). Furthermore, the standard deviations are quite similar, both holding at roughly 0.1K. However, note that the LENS climate model simulations seem to jump down drastically at several points in a manner not matched by the Kalman filter. One such instance was in 1992, the year following the Mt. Pinatubo volcanic eruption.

This suggests that the LENS climate simulations are weighting a much greater impact of atmospheric aerosol cooling than the Kalman filter (at least with the blind-model-fit value of β_3).

3.4 Future Work: More Variables and Control Theory

The Kalman filter, owing to its matrix framework, has much greater potential than what has been explored so far in this thesis. In particular, the state of the climate system could be expanded to include more variables of interest. These include new variables of interest such as precipitation, variables on a regional level (such as temperature in the northern hemisphere vs southern hemisphere), or extremes in temperature rather than simply the mean. Once sensible equations are derived that give update equations for the chosen climate metrics, the model parameters and covariance matrices can be fitted using similar methods as presented in this thesis. However, I do not expect this to work with a large number of variables, as the climate behaves according to nonlinear dynamics on a regional scale, and linearity is one of the fundamental assumptions of the Kalman filter.

If it were to be implemented, geoengineering would not be conducted according to any of the prescribed GeoMIP experiments (Kravitz, Robock, et al., 2013). Rather, it would be closely monitored and continual corrections would be made to ensure the best outcome. Assuming that such an outcome can be quantified within the CESM model and approximated by some function on the variables captured by a Kalman filter state, there already exists a powerful control algorithm (Lee and Ricker, 1994). This could easily make a projection of what the climate will likely do, and generate an ideal sequence of control inputs (particularly the growth sites and quantities of coccolithophores), from within CESM: in other words, simulate not only the intervention but also the human aspects of monitoring and reacting to the intervention while it is implemented.

REFERENCES

Adli, Mazhar (2018). *The CRISPR tool kit for genome editing and beyond.* DOI: 10.1038/s41467-018-04252-2.

Austin, Harry P. et al. (2018). "Characterization and engineering of a plastic-degrading aromatic polyesterase". In: *Proceedings of the National Academy of Sciences of the United States of America* 115.19, E4350–E4357. ISSN: 10916490. DOI: 10.1073/pnas.1718804115.

Boltzmann, Ludwig (1884). "Ableitung des Stefan'schen Gesetzes, betreffend die Abhängigkeit der Wärmestrahlung von der Temperatur aus der electromagnetischen Lichttheorie". In: *Annalen der Physik* 258.6, pp. 291–294. DOI: 10.1002/andp.18842580616.

Brett, Genevieve et al. (2020). "Biological Impacts of Physics through Idealized Tracers: Changes in the seasonal cycle of vertical exchange from early to late 21st century". In: DOI: 10.1002/ESSOAR.10502629.1.

Carvalho, Ana Sofia et al. (2018). "Ethical decision making in pain management: A conceptual framework". In: *Journal of Pain Research* 11, pp. 967–976. ISSN: 11787090. DOI: 10.2147/JPR.S162926.

Cox, H. (1964). "On the Estimation of State Variables and Parameters for Noisy Dynamic Systems". In: *IEEE Trans. Autom. Control* AC-9, pp. 5–12.

Crook, Julia A., Lawrence S. Jackson, and Piers M. Forster (2016). "Can increasing albedo of existing ship wakes reduce climate change?" In: *Journal of Geophysical Research: Atmospheres* 121.4, pp. 1549–1558. ISSN: 2169897X. DOI: 10.1002/2015JD024201. URL: http://doi.wiley.com/10.1002/2015JD024201.

Danabasoglu, Gokhan et al. (2012). "The CCSM4 ocean component". In: *Journal of Climate* 25.5, pp. 1361–1389. ISSN: 08948755. DOI: 10.1175/JCLI-D-11-00091.1.

Emanuel, Ezekiel J. and Linda L. Emanuel (1992). "Four Models of the Physician-Patient Relationship". In: *JAMA: The Journal of the American Medical Association* 267.16, pp. 2221–2226. ISSN: 15383598. DOI: 10.1001/jama.1992.03480160079038.

Evans, JRG et al. (2010). "Can oceanic foams limit global warming?" In: *Climate Research* 42.2, pp. 155–160. ISSN: 0936-577X. DOI: 10.3354/cr00885.

Fairbrother, Malcolm (2016). "Geoengineering, moral hazard, and trust in climate science: evidence from a survey experiment in Britain". In: *Climatic Change* 139.3-4, pp. 477–489. ISSN: 15731480. DOI: 10.1007/s10584-016-1818-7. URL: https://link.springer.com/article/10.1007/s10584-016-1818-7.

Field, L. et al. (2018). "Increasing Arctic Sea Ice Albedo Using Localized Reversible Geoengineering". In: *Earth's Future* 6.6, pp. 882–901. ISSN: 23284277. DOI: 10.1029/2018EF000820. URL: http://doi.wiley.com/10.1029/2018EF000820.

Friedlingstein, Pierre et al. (2019). "Global carbon budget 2019". In: *Earth System Science Data* 11.4, pp. 1783–1838. ISSN: 18663516. DOI: 10.5194/essd-11-1783-2019.

Gabriel, Corey J. et al. (2017). "The G4Foam Experiment: global climate impacts of regional ocean albedo modification". In: *Atmospheric Chemistry and Physics* 17.1, pp. 595–613. ISSN: 1680-7324. DOI: 10.5194/acp-17-595-2017. URL: https://www.atmos-chem-phys.net/17/595/2017/.

Geisen, Markus et al. (2004). "Species level variation in coccolithophores". In: *Coccolithophores*. Springer Berlin Heidelberg, pp. 327–366. DOI: 10.1007/978-3-662-06278-4{_}13.

Gent, Peter R. and Gokhan Danabasoglu (2011). "Response to Increasing Southern Hemisphere Winds in CCSM4". In: *Journal of Climate* 24.19, pp. 4992–4998. ISSN: 0894-8755. DOI: 10.1175/JCLI-D-10-05011.1. URL: http://journals.ametsoc.org/doi/10.1175/JCLI-D-10-05011.1.

Gustafsson, Bertil, Heinz-Otto Kreiss, and Joseph Oliger (2013). *Time-Dependent Problems and Difference Methods*. Hoboken, NJ, USA: John Wiley & Sons, Inc. ISBN: 9781118548448. DOI: 10.1002/9781118548448. URL: http://doi.wiley.com/10.1002/9781118548448.

Hall, Timothy M. and Darryn W. Waugh (1997). "Timescales for the stratospheric circulation derived from tracers". In: *Journal of Geophysical Research Atmospheres* 102.7, pp. 8991–9001. ISSN: 01480227. DOI: 10.1029/96jd03713.

He, Jian et al. (2015). "Decadal simulation and comprehensive evaluation of CESM/CAM5.1 with advanced chemistry, aerosol microphysics, and aerosol-cloud interactions". In: *Journal of Advances in Modeling Earth Systems* 7.1, pp. 110–141. ISSN: 19422466. DOI: 10.1002/2014MS000360. URL: http://doi.wiley.com/10.1002/2014MS000360.

Hu, Shineng and Alexey V. Fedorov (2017). "The extreme El Niño of 2015-2016 and the end of global warming hiatus". In: *Geophysical Research Letters* 44.8, pp. 3816–3824. ISSN: 00948276. DOI: 10.1002/2017GL072908. URL: http://doi.wiley.com/10.1002/2017GL072908.

Jasinski, Stephen (2020). *Phosphate Rock Statistics and Information*. Tech. rep. US Geological Survey. URL: https://www.usgs.gov/centers/nmic/phosphate-rock-statistics-and-information.

Jin, Zhonghai, Thomas P. Charlock, Ken Rutledge, et al. (2006). "Analytical solution of radiative transfer in the coupled atmosphere-ocean system with a rough surface". In: *Applied Optics* 45.28, pp. 7443–7455. ISSN: 15394522. DOI: 10.1364/AO.45.007443.

Jin, Zhonghai, Thomas P. Charlock, William L. Smith, et al. (2004). "A parameterization of ocean surface albedo". In: *Geophysical Research Letters* 31.22, pp. 1–4. ISSN: 00948276. DOI: 10.1029/2004GL021180.

Jin, Zhonghai, Yanli Qiao, et al. (2011). "A new parameterization of spectral and broadband ocean surface albedo". In: *Optics Express* 19.27, p. 26429. ISSN: 1094-4087. DOI: 10.1364/oe.19.026429.

Jones, D. D. and M. Jost (1971). "Characterization of the protein from gas-vacuole membranes of the blue-green alga, Microcystis aeruginosa". In: *Planta* 100.4, pp. 277–287. ISSN: 00320935. DOI: 10.1007/BF00385192.

Kalman, Rudolph Emil (1960). "A New Approach to Linear Filtering and Prediction Problems". In: *Transactions of the ASME–Journal of Basic Engineering* 82.Series D, pp. 35–45.

Kay, J. E. et al. (2015). "The community earth system model (CESM) large ensemble project : A community resource for studying climate change in the presence of internal climate variability". In: *Bulletin of the American Meteorological Society* 96.8, pp. 1333–1349. ISSN: 00030007. DOI: 10.1175/BAMS-D-13-00255.1.

Keith, David W. et al. (2016). "Stratospheric solar geoengineering without ozone loss". In: *Proceedings of the National Academy of Sciences of the United States of America* 113.52, pp. 14910–14914. ISSN: 10916490. DOI: 10.1073/pnas.1615572113.

Kopp, Greg and Judith L. Lean (2011). "A new, lower value of total solar irradiance: Evidence and climate significance". In: *Geophysical Research Letters* 38.1, p. L01706. ISSN: 00948276. DOI: 10.1029/2010GL045777.

Kopp, R. E. and R. J Oxford (1963). "Linear Regression Applied to System Identification and Adaptive Control System". In: *AIAA Journal* 1.10, pp. 2300–2306.

Kravitz, Ben, Philip J. Rasch, et al. (2018). "The climate effects of increasing ocean albedo: an idealized representation of solar geoengineering". In: *Atmospheric Chemistry and Physics* 18.17, pp. 13097–13113. ISSN: 1680-7324. DOI: 10.5194/acp-18-13097-2018. URL: https://www.atmos-chem-phys.net/18/13097/2018/.

Kravitz, Ben, Alan Robock, et al. (2013). "An overview of the Geoengineering Model Intercomparison Project (GeoMIP)". In: *Journal of Geophysical Research: Atmospheres* 118.23, pp. 103–13. ISSN: 2169897X. DOI: 10.1002/2013JD020569. URL: http://doi.wiley.com/10.1002/2013JD020569.

Kulski, Jerzy K. (2016). "Next-Generation Sequencing — An Overview of the History, Tools, and "Omic" Applications". In: *Next Generation Sequencing - Advances, Applications and Challenges*. InTech. DOI: 10.5772/61964.

Lee, Jay H. and N. Lawrence Ricker (1994). "Extended Kalman Filter Based Nonlinear Model Predictive Control". In: *Industrial and Engineering Chemistry Research* 33.6, pp. 1530–1541. ISSN: 15205045. DOI: 10.1021/ie00030a013. URL: https://pubs.acs.org/doi/abs/10.1021/ie00030a013.

Lin, Albert C (2013). "Does Geoengineering Present a Moral Hazard?" In: *Ecology Law Quarterly* 40.3, pp. 673–711. URL: https://escholarship.org/uc/item/7th0d0pd.

Loeb, Norman G., John M. Lyman, et al. (2012). "Observed changes in top-of-the-atmosphere radiation and upper-ocean heating consistent within uncertainty". In: *Nature Geoscience* 5.2, pp. 110–113. ISSN: 17520894. DOI: 10.1038/ngeo1375.

Loeb, Norman G., Bruce A. Wielicki, et al. (2007). "Variability in global top-of-atmosphere shortwave radiation between 2000 and 2005". In: *Geophysical Research Letters* 34.3, p. L03704. ISSN: 0094-8276. DOI: 10.1029/2006GL028196. URL: http://doi.wiley.com/10.1029/2006GL028196.

Masson-Delmotte, V et al. (2018). "Global Warming of 1.5 C. An IPCC Special Report on the Impacts of Global Warming of 1.5 C Above Pre-Industrial Levels and Related Global Greenhouse ..." In:

McCusker, Kelly E et al. (2014). "Rapid and extensive warming following cessation of solar radiation management". In: *Environmental Research Letters* 9.2, p. 024005. ISSN: 1748-9326. DOI: 10.1088/1748-9326/9/2/024005. URL: https://iopscience.iop.org/article/10.1088/1748-9326/9/2/024005.

Morét-Ferguson, Skye et al. (2010). "The size, mass, and composition of plastic debris in the western North Atlantic Ocean". In: *Marine Pollution Bulletin* 60.10, pp. 1873–1878. ISSN: 0025326X. DOI: 10.1016/j.marpolbul.2010.07.020.

Morice, Colin P. et al. (2012). "Quantifying uncertainties in global and regional temperature change using an ensemble of observational estimates: The HadCRUT4 data set". In: *Journal of Geophysical Research: Atmospheres* 117.D8, n/a–n/a. ISSN: 01480227. DOI: 10.1029/2011JD017187. URL: http://doi.wiley.com/10.1029/2011JD017187.

Olhoff, Anne and John M Christensen (2019). *Emissions Gap Report 2019: A UNEP Synthesis Report*. Nairobi: United Nations Environment Programme. ISBN: 978-92-807-3766-0. URL: www.unenvironment.org/resources/emissions-gap-report.

Pan, Laura L. et al. (2016). "Transport of chemical tracers from the boundary layer to stratosphere associated with the dynamics of the Asian summer monsoon". In: *Journal of Geophysical Research: Atmospheres* 121.23, pp. 159–14. ISSN: 2169897X. DOI: 10.1002/2016JD025616. URL: http://doi.wiley.com/10.1002/2016JD025616.

Parker, Andy and Peter J. Irvine (2018). "The Risk of Termination Shock From Solar Geoengineering". In: *Earth's Future* 6.3, pp. 456–467. ISSN: 23284277. DOI: 10.1002/2017EF000735. URL: http://doi.wiley.com/10.1002/2017EF000735.

Pistone, Kristina, Ian Eisenman, and V. Ramanathan (2014). "Observational determination of albedo decrease caused by vanishing Arctic sea ice". In: *Proceedings of the National Academy of Sciences of the United States of America* 111.9, pp. 3322–3326. ISSN: 00278424. DOI: 10.1073/pnas.1318201111.

Polovina, Jeffrey J., Evan A. Howell, and Melanie Abecassis (2008). "Ocean's least productive waters are expanding". In: *Geophysical Research Letters* 35.3, p. L03618. ISSN: 0094-8276. DOI: 10.1029/2007GL031745. URL: http://doi.wiley.com/10.1029/2007GL031745.

Rauch, H. E., F. Tung, and C. T. Striebel (1965). "Maximum likelihood estimates of linear dynamic systems". In: *AIAA Journal* 3.8, pp. 1445–1450. DOI: 10.2514/3.3166. eprint: https://doi.org/10.2514/3.3166. URL: https://doi.org/10.2514/3.3166.

Robock, Alan (2008). "20 reasons why geoengineering may be a bad idea". In: *Bulletin of the Atomic Scientists* 64.2, pp. 14–18. ISSN: 0096-3402. DOI: 10.2968/064002006. URL: http://thebulletin.metapress.com/openurl.asp?genre=article&id=doi:10.2968/064002006.

Rougier, Jonathan and Michael Goldstein (2014). "Climate Simulators and Climate Projections". In: *Annual Review of Statistics and Its Application* 1.1, pp. 103–123. ISSN: 2326-8298. DOI: 10.1146/annurev-statistics-022513-115652. URL: http://www.annualreviews.org/doi/10.1146/annurev-statistics-022513-115652.

Sato, M. et al. (1993). "Stratospheric aerosol optical depths, 1850-1990". In: *Journal of Geophysical Research* 98.D12. ISSN: 01480227. DOI: 10.1029/93jd02553.

Schwartz, Stephen E. (2007). "Heat capacity, time constant, and sensitivity of Earth's climate system". In: *Journal of Geophysical Research* 112.D24, D24S05. ISSN: 0148-0227. DOI: 10.1029/2007JD008746. URL: http://doi.wiley.com/10.1029/2007JD008746.

Sebille, Erik van et al. (2015). "A global inventory of small floating plastic debris". In: *Environmental Research Letters* 10.12, p. 124006. ISSN: 1748-9326. DOI: 10.1088/1748-9326/10/12/124006. URL: https://iopscience.iop.org/article/10.1088/1748-9326/10/12/124006.

Seitz, Russell (2011). "Bright water: Hydrosols, water conservation and climate change". In: *Climatic Change* 105.3-4, pp. 365–381. ISSN: 01650009. DOI: 10.1007/s10584-010-9965-8.

Smith, R et al. (2010). *The Parallel Ocean Program (POP) Reference Manual Ocean Component of the Community Climate System Model (CCSM)*. Tech. rep. URL: http://cesmweb.cgd.ucar.edu/models/ccsm4.0/pop/doc/sci/POPRefManual.pdf.

Stephens, Graeme L. et al. (2015). "The albedo of Earth". In: *Reviews of Geophysics* 53.1, pp. 141–163. ISSN: 87551209. DOI: 10.1002/2014RG000449. URL: http://doi.wiley.com/10.1002/2014RG000449.

Stocker, Thomas F. et al. (2013). *Climate change 2013 the physical science basis: Working Group I contribution to the fifth assessment report of the intergovernmental panel on climate change*. Vol. 9781107057999. Cambridge University Press, pp. 1–1535. ISBN: 9781107415324. DOI: 10.1017/CBO9781107415324.

Taylor, Alison R. (2011). "A scanning electron micrograph of a single coccolithophore cell. " In: *PLOS Biology* 9.6, ev09.i06. ISSN: 1545-7885. DOI: 10.1371/IMAGE.PBIO.V09.I06.

Tournier, V. et al. (2020). "An engineered PET depolymerase to break down and recycle plastic bottles". In: *Nature* 580.7802, pp. 216–219. ISSN: 0028-0836. DOI: 10.1038/s41586-020-2149-4. URL: http://www.nature.com/articles/s41586-020-2149-4.

Tyrrell, T., P. M. Holligan, and C. D. Mobley (1999). "Optical impacts of oceanic coccolithophore blooms". In: *Journal of Geophysical Research: Oceans* 104.C2, pp. 3223–3241. ISSN: 2169-9291. DOI: 10.1029/1998jc900052.

Vernier, J. P. et al. (2011). "Major influence of tropical volcanic eruptions on the stratospheric aerosol layer during the last decade". In: *Geophysical Research Letters* 38.12. ISSN: 00948276. DOI: 10.1029/2011GL047563.

Wan, E. A. and R. Van Der Merwe (2000). "The unscented Kalman filter for nonlinear estimation". In: *IEEE 2000 Adaptive Systems for Signal Processing, Communications, and Control Symposium, AS-SPCC 2000*. Institute of Electrical and Electronics Engineers Inc., pp. 153–158. ISBN: 0780358007. DOI: 10.1109/ASSPCC.2000.882463.

Wang, Y.-M., J. L. Lean, and N. R. Sheeley Jr. (2005). "Modeling the Sun's Magnetic Field and Irradiance since 1713". In: *The Astrophysical Journal* 625.1, pp. 522–538. ISSN: 0004-637X. DOI: 10.1086/429689.

Wielicki, Bruce A. et al. (1996). "Clouds and the Earth's Radiant Energy System (CERES): An Earth Observing System Experiment." In: *BAMS* 77.5, pp. 853–868. DOI: 10.1175/1520-0477(1996)077<0853:CATERE>2.0.CO;2.

Willson, Richard C. and Hugh S. Hudson (1991). "The Sun's luminosity over a complete solar cycle". In: *Nature* 351.6321, pp. 42–44. ISSN: 00280836. DOI: 10.1038/351042a0.

(WMO), World Meteorological Organization (2017). *WMO Guidelines on the Calculation of Climate Normals*. 2017 edition. WMO. Geneva: WMO. ISBN: 978-92-63-11203-3.

Zhang, Hongrui et al. (2018). "Technical note: A refinement of coccolith separation methods: measuring the sinking characteristics of coccoliths". In: *Biogeosciences* 15.15, pp. 4759–4775. ISSN: 1726-4189. DOI: 10.5194/bg-15-4759-2018. URL: https://www.biogeosciences.net/15/4759/2018/.

Zhang, Yorke et al. (2017). "A semi-synthetic organism that stores and retrieves increased genetic information". In: *Nature* 551.7682, pp. 644–647. ISSN: 14764687. DOI: 10.1038/nature24659.

Zheng, Mei Di and Long Cao (2014). "Simulation of global ocean acidification and chemical habitats of shallow- and cold-water coral reefs". In: *Advances in Climate Change Research* 5.4, pp. 189–196. ISSN: 16749278. DOI: 10.1016/j.accre.2015.05.002.

Zhong, Wenyi and Joanna D. Haigh (2013). "The greenhouse effect and carbon dioxide". In: *Weather* 68.4, pp. 100–105. ISSN: 00431656. DOI: 10.1002/wea.2072. URL: http://doi.wiley.com/10.1002/wea.2072.

APPENDIX

Appendix A

A.1 Glossary of Symbols

Symbol	Description	Units [Range]
R^2	Coefficient of determination: fraction of variance explained by the model	[0,1]
σ	Standard deviation ($\sqrt{Var}$)	
n	Time index	Years
k	Time step	1 year
T	Temperature at Earth's surface (global average when scalar-valued)	Kelvin
$_{30} < T >$	30-year running average of the temperature ($\pm$15 years from that date), a standard measure of climate	Kelvin
$albedo$	Fraction of incident light that is reflected by a surface	[0,1]
E	Radiating Energy (various subscripts)	W/m^2
SW_{in}	Sun-to-earth short-wave radiation that is absorbed as heat at Earth's surface	W/m^2
LW_{out}	Earth-to-space long-wave radiation that fully escapes the atmosphere	W/m^2
Sol_{rad}	The average solar insolation that shines per unit area on average at the top of Earth's atmosphere	341 W/m^2
b	Water particle scattering coefficient, which increases linearly with mass load	m^{-1}
τ	Atmospheric aerosol depth	[0,1]
$[Chl]$	Water Chlorophyll concentration	mg/m^3
$[CO_2]$	Atmospheric carbon dioxide concentration	ppm
∂C	Mass of carbon emitted by human activities in one year	gigatonnes
C_{heat}	Heat capacity of the average parcel of the Earth's surface	W / m^2 * year / K
σ_{sb}	Stefan–Boltzmann constant	$5.670 * 10^{-8}$ W m^{-2} K^{-4}
β_0	Constant fraction of LW light that is radiated from the surfaced and then back-scattered by atmosphere in the absence of CO_2	≈ 0.05
β_1	Coefficient of $log_{10}[CO_2]$ that determines the potency of back-scattering	≈ 0.2
β_2	Constant fraction of SW light that is reflected by the atmosphere and Earth's surface before it turns into heat in the absence of atmospheric aerosols	0.29
β_3	Adjustment factor of the atmospheric aerosol depth that determines what fraction of the top of these sooty particle clouds reflect away all the light that this layer blocks	$\approx 5 * 10^{-5}$

A.2 Potential (Commercial) Benefits

Renewable Mining of Phosphates

Over 70% of the world's proven reserves of phosphates (an essential feed-stock for modern agriculture) is located in Morocco and the Western Sahara, a geopolitically concerning monopoly. Moreover, global reserves will be exhausted by 2400 at current usage rates (Jasinski, 2020). Skimming concentrated coccolithophores could be a renewable source.

Preservation of Arctic Sea Ice

A recently published experiment has demonstrated that multi-year Arctic Sea Ice might be preserved by coating the surface of fresh ice in hollow glass spheres only a few dozen micrometers in diameter (Field et al., 2018). The fossilized floating coccolithophores might be quite similar in physical properties to these glass micro-bead, hence they could be transported north and used to seed specific ice floes.

Targeting Plastic Microparticles

There has been significant concern regarding the steadily accumulating plastic trash from the biosphere. The vast majority of this trash is on the scale of 3mm and sparsely dispersed throughout the ocean (Morét-Ferguson et al., 2010). Perhaps the coccolithophores could serve as a delivery vector to chemically recognize plastic microparticles and target them with potent catabolic enzymes (Austin et al., 2018; Tournier et al., 2020) before they enter the aquatic food chain. On a basic science level, the following simulations allow for predictions of the future distributions of micro-plastics under different climate scenarios.

Appendix B

B.1 Buoyancy Simulation - Simplified Example

To simplify, we begin by assigning the water column to the interval [0,L], where L is the ocean floor and 0 is the surface, both with insulated Neumann boundary conditions.

$$u_t = au_x + \frac{\partial}{\partial x}(\eta(x)u_x) \tag{B.1}$$

Within the CESM model, this equation is solved for both $\eta(x)$ and u within the continuously evolving ocean grid. But I will substitute in an example function of $\eta(x)$. Owing to the mixing effects of wave action, we assume that the diffusion increases exponentially as one approaches the mixed layer, and therefore exponentially decays with depth.

$$\begin{cases} u_t = au_x + (be^{c(L-x)} + d)u_{xx} & \text{for} \quad (x,t) \in (0,L) \times (0,\infty) \\ u_x = 0 & \text{for} \quad (x,t) \in \{0,L\} \times (0,\infty) \end{cases} \tag{B.2}$$

Each of these coefficients requires an explanation and a way to experimentally determine them. a is simple: just measure the rate at which the band of particles with the highest density rises in still water. To determine the coefficients that determine the rate of diffusion, I will change the coefficents b and d, allowing me to rewrite the magnitude of u_{xx}.

$$b = \frac{\tilde{b}}{e^{cL} - 1} \qquad \tilde{b} = b(e^{cL} - 1) \tag{B.3}$$

$$d = \tilde{d} - b = \frac{\tilde{b}}{e^{cL} - 1} \qquad \tilde{d} = d + b \tag{B.4}$$

$$be^{c(L-x)} + d = \tilde{b}\frac{e^{c(L-x)} + 1}{e^{cL} - 1} + \tilde{d} \tag{B.5}$$

With this change, $\tilde{d}$ is seen to be diffusion rate at the ocean floor ($x = L$), which can be measured using neutrally buoyant but appropriately sized particles placed in still water. $\tilde{b} + \tilde{d}$ is the corresponding the diffusion rate at the ocean surface, and can be measured similarly by diffusing neutrally buoyant particles in turbulent water with surface waves. The difference between these two diffusion rates yields $\tilde{b}$.

c has to do with the rate at which mixing (and thus diffusion) increases as one approaches the surface. The simplest way to measure it is to find the ocean depth $\delta_{0.5}$ at which neutrally buoyant particles will diffuse at the rate midway between that measured at the surface, $\tilde{b}+\tilde{d}$, and that measured at conditions mimicking the ocean floor, $\tilde{d}$. At this specific depth, the diffusion rate is:

$$\begin{aligned}
\tilde{b}\frac{e^{c(L-\delta_{0.5})}+1}{e^{cL}-1} + \tilde{d} &= \frac{\tilde{b}+2\tilde{d}}{2} \\
\frac{e^{c(L-\delta_{0.5})}+1}{e^{cL}-1} &= \frac{1}{2} \\
2e^{c(L-\delta_{0.5})} &= e^{cL}+1 \\
e^{c\delta_{0.5}} &= \frac{2e^{cL}}{e^{cL}+1} \\
\delta_{0.5} &= L + \ln\frac{2}{e^{cL}+1}
\end{aligned} \tag{B.6}$$

Obtaining the value of c from $\delta_{0.5}$ just requires inverting this transcendental function. But the actual function for $\eta(x)$ is much more complicated and is computed automatically within CESM.

B.2 Numerical Scheme of Advection-Diffusion

. To describe the numerical scheme used to compute the advection-diffusion of buoyant particles, I will adopt the notation of Time-Dependent Problems and Difference Methods (Gustafsson, Kreiss, and Oliger, 2013). To recapitulate their work in Section 1.7, I will

begin with the boundary-less convection-diffusion equation:

$$\begin{cases} u_t + \alpha u_x = \eta u_{xx} & \text{for} \quad (x,t) \in (0,L) \times (0,\infty) \\ u(x,0) = f(x) & \text{for} \quad x \in (0,L) \end{cases} \tag{B.7}$$

The simplest explicit difference approximation is

$$v_j^{n+1} = v_j^n + k(\eta D_+ D_- - \alpha D_0) v_j^n, \quad j = 0, 1, ..., N. \tag{B.8}$$

$$v_j^{n+1} = v_j^n + \frac{k\eta}{h^2}(v_{j+1}^n - 2v_j^n + v_{j-1}^n) + \frac{k\alpha}{2h}(-v_{j+1}^n + v_{j-1}^n) \tag{B.9}$$

$$v_j^{n+1} = (\frac{k\eta}{h^2} - \frac{k\alpha}{2h})v_{j+1}^n + (1 - 2\frac{k\eta}{h^2})v_j^n + (\frac{k\eta}{h^2} + \frac{k\alpha}{2h})v_{j-1}^n \tag{B.10}$$

Note that if $2\eta = h\alpha$ then this becomes a two-point scheme, as v_{j+1}^n drops out.

$$v_j^{n+1} = (1 - \frac{k\alpha}{h})v_j^n + (\frac{k\alpha}{h})v_{j-1}^n \tag{B.11}$$

This is what Dr. Jay Brett assumed in her code (and I currently have implemented). Now, to determine the stability region, the amplification factor in Fourier space is:

$$\hat{Q} = 1 - 2\beta sin^2\frac{\zeta}{2} - i\lambda \sin\zeta, \quad \zeta = \omega h, \quad \beta = \frac{2\eta k}{h^2}, \quad \lambda = \frac{\alpha k}{h} \tag{B.12}$$

$$\begin{aligned} \left|\hat{Q}^2\right| &= 1 - 4\beta sin^2\frac{\zeta}{2} + 4\beta^2 sin^4\frac{\zeta}{2} + 4\lambda^2 \sin^2\frac{\zeta}{2}\left(1 - sin^2\frac{\zeta}{2}\right) \\ &= 1 - 4(\lambda^2 + \beta^2)s^2 + 4(\lambda^2 - \beta)s, \quad s = sin^2\frac{\zeta}{2} \end{aligned} \tag{B.13}$$

$$\text{Stability requires} \qquad |\hat{Q}| \leq 1 \qquad \forall\zeta \tag{B.14}$$

$$-4(\lambda^2 + \beta^2)s^2 + 4(\lambda^2 - \beta)s \leq 0 \qquad \forall s \in [0,1] \tag{B.15}$$

$$-(\lambda^2 + \beta^2)s + (\lambda^2 - \beta) \leq 0 \qquad \forall s \in [0,1] \tag{B.16}$$

$$\lambda^2 - \beta \leq 0, \quad \text{and} \quad \beta(\beta - 1) \leq 0 \tag{B.17}$$

$$\lambda^2 \leq \beta \leq 1, \quad \text{or} \quad \alpha^2 k \leq 2\eta \leq h^2/k \tag{B.18}$$

This of course assumes that the spacial grid size k and the diffusion constant η are both constant. In fact, both are not constant: $1/k$ and η both increase substantially as $x \to 0$.

To estimate the truncation error, we calculate how well the exact solution u satisfies the difference scheme:

$$\begin{aligned}\tau_j^n := \frac{u_j^{n+1} - u_j^n}{k} - (\eta D_+ D_- - \alpha D_0) u_j^n &= u_t(x_j, t_n) + \frac{k}{2} u_{tt}(x_j, \zeta_t^1) \\ &\quad + \alpha u_x(x_j, t_n) + \alpha \frac{h^2}{3!} u_{xx}(\zeta_x^1, t_n) \\ &\quad - \eta u_{xx}(x_j, t_n) - \eta \frac{2h^2}{4!} u_{xxxx}(\zeta_x^2, t_n) \qquad \text{(B.19)}\end{aligned}$$

$$\text{where} \quad \zeta_x^1, \zeta_x^2 \in [x_j - h, x_j + h] \quad \text{and} \quad \zeta_t^1 \in [t_n, t_n + k]$$

$$\text{By definition of } u, \quad u_t - \alpha u_x - \eta u_{xx} = 0$$

$$\tau_j^n = k \frac{u_{tt}(x_j, \zeta_t^1)}{2} + h^2 \big(\frac{\alpha}{3!} u_{xx}(\zeta_x^1, t_n) - \frac{2\eta}{4!} u_{xxxx}(\zeta_x^2, t_n) \big) \qquad \text{(B.20)}$$

This difference operator is first order in time and second order in space.

In the CESM model, the values of η, k actually vary with depth. Such a nonlinear differential equation is much more difficult to analyze, and is beyond the scope of this undergraduate thesis.

B.3 COART Emulator

As explained in the main body of the thesis, a custom emulator of the COART light flux model (Jin, Charlock, Rutledge, et al., 2006) was created by interpolating functions for both the albedo and top-layer absorbance. First, an online version of the COART model was utilized to calculate both of these outputs (in (W/m2)) relative to the incident light across the integrated spectrum from to 0.25 to 4.0 um at a spectral resolution of 0.15 um. Outputs were calculated at solar zenith angles from 0° to 87.5° with a step of 2.5° using a layered atmosphere with no change to CO_2 nor CH_4. MODTRAN Maritime mixed-layer atmospheric aerosols were included at an aerosol optical thickness of 0.2 at 0.5 um, but no clouds nor stratospheric aerosols were selected to be present. The default absorption parameterizations of overall absorbance, absorbance of dissolved organic matter, and surface roughness were

used. The default ocean conditions were not modified (no wind, 100m deep, 0.1 bottom albedo), but chlorophyll concentrations ($[Chl]$) of 0, 0.2, 2, 20, and 200 mg/m^3 were tested. Most importantly, the particle scattering coefficient b was modified to be constant across wavelengths and chlorophyll concentrations by setting the exponents n and k to 0. b was tested at values of 0, 0.05, 0.5, 1, 5, 20, 50, 100, and 200 for each $[Chl]$. The COART model crashed at the highest values of $[Chl]$ and b together, so this simulation was discarded. Note that in the process of building this emulator, I made an error in originally designing it to calculate the albedo and top-layer (5m) absorbance for the combination of diffuse and direct light. Later, this emulator was later used for only the direct light (the diffuse light was calculated at $\cos z = 0.67$) and across a top-layer which was 10m thick in total (5m center). As direct light constitutes the vast majority of heat flux and the effects of the absorbing particles $[Chl]$ were not further investigated, for the purposes of this thesis, this emulator is sufficient.

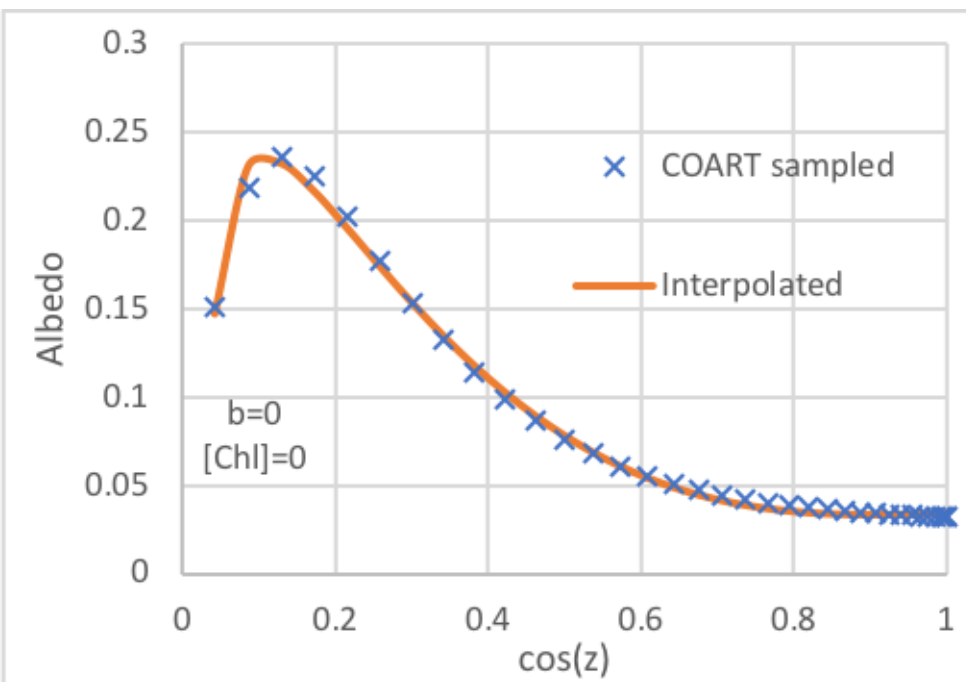

Figure B.1 Both the samples from the COART model and the interpolated function from Eq. B.21 at $b = 0$ and $[Chl] = 0$.

First, an emulator for albedo was built. The following function of solar zenith angle z was interpolated for each COART simulation, as illustrated in the example Figure B.1:

$$albedo(z; [Chl], b) = -s_3/\cos z + s_4 * (\cos z)^{s_1} + s_2 \tag{B.21}$$

Next, the values of these four coefficients $s_{1..4}$ were interpolated for all values of b at one $[Chl]$, as illustrated in Figure B.2:

$$s_1(b; [Chl]) = r_{1,1} * b + r_{1,2} + r_{1,3} * \exp(r_{0,4} * b) \tag{B.22}$$

$$s_x(b; [Chl]) = \log(r_{x,4} * b + r_{x,3}) * r_{x,1} + r_{x,2} \quad for \quad x = 2..4 \tag{B.23}$$

$$r_{2,4} = 1 \quad and \quad r_{4,4} = 1 \tag{B.24}$$

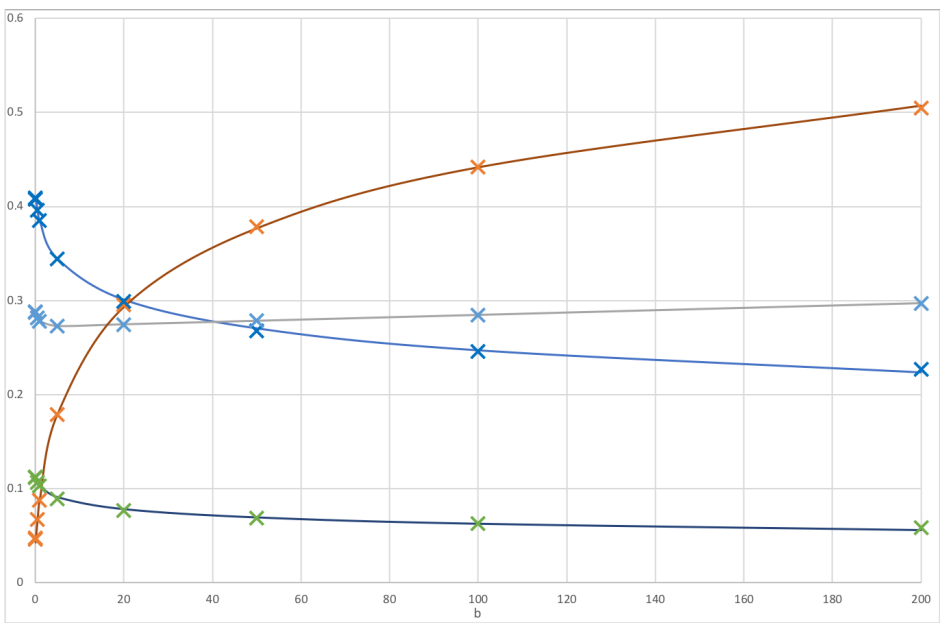

Figure B.2 Both the fit values of $s_{1..4}$ in X's and the interpolated functions in lines involving $r_{1..4,1..4}$ from Eqs. B.22 to B.23 at $[Chl] = 0$. Note that the values of $s_2/10$ and $s_4 * 10$ are plotted so that all s parameters can be visualized on this graph.

This process was repeated once more to find the values of each r at a given $[Chl]$, but this process involved 14 functions of 5 different forms (each taking 3 parameters). These innermost functions are both typeset in Eqs. B.25 to B.29 and can be read in the FORTRAN

code attached below. Which innermost function is used for which r coefficient and the parameters for these functions are included in the arrays at the beginning of this code.

$$f_1([Chl]) = \exp\left(q_1 * \log_{10}[Chl] + q_3 * (\log_1 0[Chl])^2\right) * q_2 \tag{B.25}$$

$$f_2([Chl]) = q_1 * \log_{10}[Chl] + q_3 * (\log_{10}[Chl])^2 + q_2 \tag{B.26}$$

$$f_3([Chl]) = q_1 + \exp(\log_{10}[Chl] * q_3) * q_2 \tag{B.27}$$

$$f_4([Chl]) = q_1 + \exp(-[Chl] * q_3) * q_2 \tag{B.28}$$

$$f_5([Chl]) = \exp(-[Chl]) * q_1 + \exp(-[Chl] * q_3) * q_2 \tag{B.29}$$

Regarding the light which is absorbed in the first 10 m of ocean, this process was repeated, noting that the fraction of absorbed light (even after removing that reflected by the albedo) is strongly correlated with that albedo:

$$absorb(z; [Chl], b) = s_5 * (cos(z)^2 - cos(z)) - s_6 * albedo(z; [Chl], b) + s_7 \tag{B.30}$$

Likewise functions were fit for these values of $s_{4..6}$ across the range of b at each $[Chl]$:

$$s_5(b; [Chl]) = r_{5,1} * \exp(-|b - r_{5,2}|/r_{5,3}) + r_{5,4} \tag{B.31}$$

$$s_x(b; [Chl]) = 1 - r_{x,2} * \exp(-r_{x,1} * b) \quad for \quad x = 6..7 \tag{B.32}$$

These r coefficients were again interpolated between $[Chl]$ values using Eqs. B.25 to B.29.

```
module calculator
  implicit none
  integer,parameter,dimension(24) :: ctlFxn = (/1,2,2,1,3,3,1,0,&
                3,2,2,1,2,2,1,0,2,3,2,2,2,4,2,5/)
  real*8,parameter,dimension(24) :: ctlParA = (/-0.2752494740,-0.0458254151,&
0.0446303901,-0.5683269568,0.2008671625,-0.0618870089,0.2001849426,0.0000000000,&
0.0020402023,0.0002018875,0.0190378343,-0.0439122887,&
0.0079686198,0.0057858173,0.3916968146,0.0000000000,&
0.002629367,0.240014106,1.786102093,0.029601102,&
-0.003974811,0.008501399,0.021081096,0.090088604/)
  real*8,parameter,dimension(24) :: ctlParB = (/0.0012350808,2.7210535980,&
0.1581961254,1.0656261587,0.0199618556,0.0637922964,1.6937910519,0.0000000000,&
0.0001699326,0.0110000303,0.8390846756,1.3000844189,&
0.0781324491,0.4055948942,0.8412616011,0.0000000000,&
-0.144772187,2.171705306,2.815379622,-0.034692206,&
0.05727732,0.367410471,0.04091918,0.267622484/)
  real*8,parameter,dimension(24) :: ctlParC = (/-0.2997132408,-0.0111000437,&
0.0102728755,-0.1236148245,0.5481961977,0.6136596117,0.1926497173,0.0000000000,&
0.5935329753,0.0000002593,0.0037620190,-0.2182911532,&
0.0012999933,0.0119173776,0.1476701059,0.0000000000,&
0.004552898,-0.946005249,-0.497443432,-0.005623273,&
0.032046079,0.039385742,0.020637421,0.049758211/)

!note - not as in excel sheet, last 4 are switched so that the exponential 2x2 is at the end
contains

subroutine compute_chl_coeff(chl,values)
  real*8, intent(in):: chl
  real*8,dimension(24), intent(out):: values
```

```
! compute the lowest-level parameter values based on the amount of chlorophyll
  integer :: i, indexFxn
  real*8 :: logchl

  do i = 1,24

  indexFxn=ctlFxn(i)
! pick which function we are using
  if (chl<0.02) then
     logchl=0.0
  else
     logchl=LOG10(chl/2)+2
  end if

  SELECT CASE(indexFxn)
     CASE(1)
          values(i)=EXP( ctlParA(i)*logchl+ctlParC(i)*logchl**2 )*ctlParB(i)
     CASE(2)
          values(i)= ctlParA(i)*logchl+ctlParC(i)*logchl**2 + ctlParB(i)
     CASE(3)
          values(i)= ctlParA(i) + EXP(ctlParC(i)*logchl)*ctlParB(i)
     CASE(4)
          values(i)= ctlParA(i) + EXP(-ctlParC(i)*chl)*ctlParB(i)
     CASE(5)
          values(i)= ctlParA(i)*EXP(-chl) + EXP(-ctlParC(i)*chl)*ctlParB(i)
     CASE DEFAULT
          values(i) = 1.0
   END SELECT
   end do
 end subroutine compute_chl_coeff


  subroutine compute_bub_coeff(bub,chl,values)
    real*8, intent(in):: bub,chl
    real*8,dimension(7), intent(out):: values

    real*8,dimension(24)::allcchl
    real*8,dimension(4)::cchl
    real*8::cchl1, cchl2
    integer::k, i

    call compute_chl_coeff(chl,allcchl)

    do i = 1,7

    if (i.le.5 ) then
       do k=1,4
            cchl(k)=allcchl((i-1)*4+k)
       end do
    else
      cchl1 = allcchl(9+2*i)
      cchl2 = allcchl(10+2*i) !24=6+2*7
    end if

    SELECT CASE(i)
       CASE(1)
            values(i)= cchl(1)*bub+ cchl(2)+ cchl(3)*EXP(-cchl(4)*bub)
       CASE(2)
             values(i) = cchl(1) * LOG10(cchl(3)+bub) - cchl(2)
       CASE(3)
            values(i) = -cchl(1) * LOG10(cchl(3)+bub*cchl(4) ) + cchl(2)
       CASE(4)
             values(i) = -cchl(1) * LOG10(cchl(3)+bub) + cchl(2)
       CASE(5)
             values(i) = cchl(1) * EXP(-ABS(bub-cchl(2))/cchl(3))+cchl(4)
       CASE(6,7)
             values(i) = 1- cchl2 * EXP(-cchl1*bub)
       CASE DEFAULT
             values(i)  = 0.0
     END SELECT
    end do
  end subroutine compute_bub_coeff

 subroutine compute_top_layer(ang,blb,chl,alb, absorb)
   real*8, intent (in) :: ang,blb, chl
   real*8, intent (out) :: alb, absorb

   real*8,dimension(7)::acblb

   call compute_bub_coeff(blb,chl,acblb)

   alb = - acblb(3) /COS(ang) + acblb(4)* (1-COS(ang))**acblb(1)+acblb(2)

   absorb = acblb(7) -  alb * acblb(6) + acblb(5)*COS(ang)*(COS(ang)-1)
   !print *, acblb(7), acblb(6), acblb(5), alb, COS(ang)
   !print *, " "
 end subroutine compute_top_layer

end module calculator
```

Appendix C

C.1 Derivation of LOG[CO2]

At any one wavelength, the concentration of CO_2 is directly proportional to the absorbance, which is the exponential power of the inverse of transmittance. l is a distance factor related to the thickness of the atmosphere.

$$-\log(\frac{I_{exit}}{I_{total}}) = A = \epsilon(\gamma)l[CO_2] \tag{C.1}$$

$$I_{absorb} = I_{total} - I_{exit} = I_{total}\big(1 - \exp(-\epsilon(\gamma)l[CO_2])\big) \tag{C.2}$$

Then, over all wavelengths, the fraction of long-wave light radiating out into space that is absorbed by CO_2 is roughly normally distributed about 680 cm^{-1}.

$$\epsilon(\gamma) \approx \exp(-\frac{(\gamma - 680)^2}{\sigma^2}) \tag{C.3}$$

Integrating this absorption over all wavelengths to get the absorbed energy E rather than an intensity I at a single wavelength

$$E_{absorb} = E_{total}\int_{-\infty}^{\infty}\big(1 - \exp(-\exp(-\frac{(\gamma - 680)^2}{\sigma^2})l[CO_2])\big)d\gamma \tag{C.4}$$

$$= E_{total}\sigma\int_{-\infty}^{\infty}\big(1 - \exp(-l[CO_2]e^{(-\gamma^2)}\big)d\gamma \tag{C.5}$$

To the best of my knowledge, there is no analytical solution to this integral. However, upon inspection I observe that when $[CO_2]l$ is larger than e, this integrated function approximates a symmetric trapezoid of height 1. Thus, solving for the upper and lower fourth of this

trapezoid (as the very top and bottom are exponential limits):

$$\frac{3}{4} = \left(1 - \exp(-l[CO_2]e^{(-\gamma^2)}\right) \tag{C.6}$$

$$\gamma = \pm\sqrt{\log(\frac{l[CO_2]}{2\log(2)})} \qquad for \quad (l[CO_2]) >= 2\log(2) \tag{C.7}$$

$$\frac{1}{4} = \left(1 - \exp(-l[CO_2]e^{(-\gamma^2)}\right) \tag{C.8}$$

$$\gamma = \pm\sqrt{\log(\frac{l[CO_2]}{2\log(2) - \log(3)})} \qquad for \quad (l[CO_2]) >= 2\log(2) - \log(3) \tag{C.9}$$

$$Area = \frac{top + bottom}{2}1 \tag{C.10}$$

$$= \left(\gamma_{1+} + \gamma_{1-} + \gamma_{0+}\gamma_{0-}\right)/2 \tag{C.11}$$

$$= \left(\gamma_{1+} + \gamma_{0+}\right) \tag{C.12}$$

$$= \left(\gamma_{0.75} - \frac{\gamma_{0.25} - \gamma_{0.75}}{2}\right) + \left(\gamma_{0.25} + \frac{\gamma_{0.25} - \gamma_{0.75}}{2}\right) = \qquad \left(\gamma_{0.75} + \gamma_{0.25}\right) \tag{C.13}$$

$$= \sqrt{\log(\frac{l[CO_2]}{2\log(2)})} + \sqrt{\log(\frac{l[CO_2]}{2\log(2) - \log(3)})} \tag{C.14}$$

The logarithm within this function dominates, whereas the sum of square roots can be linearly approximated over the relevant range of CO_2 concentrations. Over a broader range of concentrations, other spectral effects at different wavelengths begin to play a major role (see Figure C.1 below).

$$E_{absorb} \approx \beta \log([CO_2])E_{total} \tag{C.15}$$

C.2 Core Kalman Filter Code

This is the Kalman filter code that was used in the MCMC search. As such, it takes the parameter values as inputs, plots nothing, and calculates the likelihood of both the data and the 30-year average states. This python code is included following Figure C.1 below.

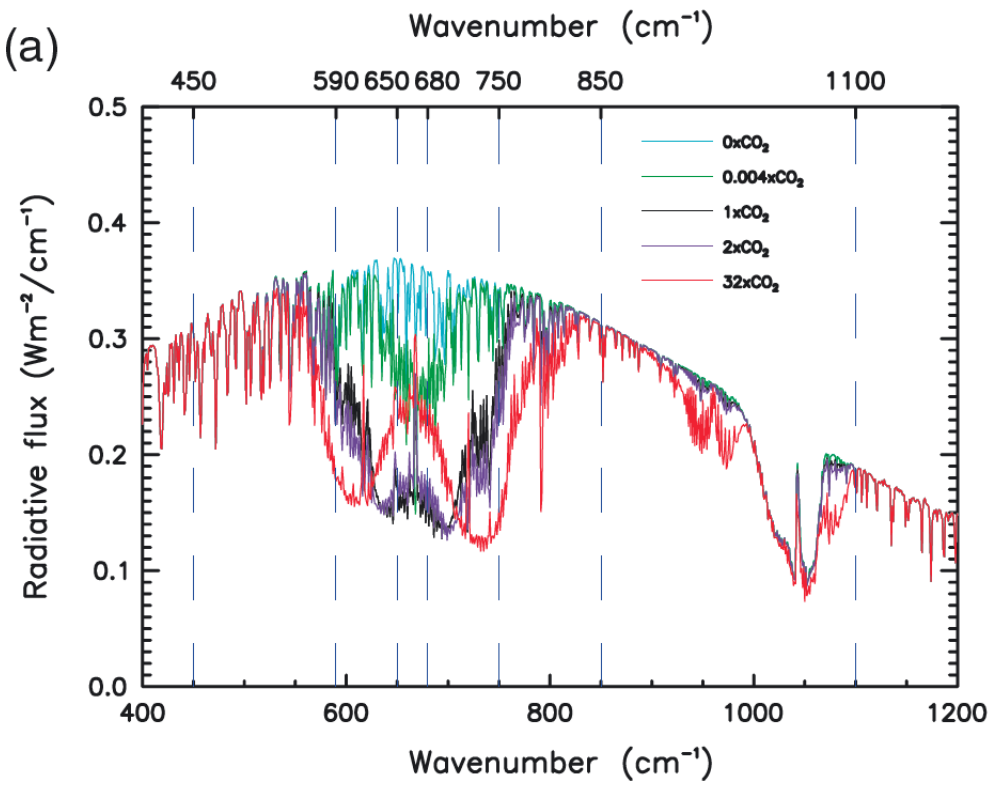

Figure C.1 The impact various concentrations of CO_2 have on the emission spectrum from Earth. Adapted from (Zhong and Haigh, 2013). Notice that before the 32xCO2 concentration, the dent in the emission spectrum behaves as a truncated Gaussian integral.

```
plimport numpy as np

def log_lik(params):
    n_iter = 170
    sz = (n_iter,1) # size of array

    data = np.genfromtxt(open("toyKFmodelData.csv", "rb"),dtype=float, delimiter=',')
    dates=data[:,0]
    dates[0]=1850
    temps=data[:, 1]+287
    lCo2=np.log10(data[:,2])

    heatwmsq=params[0]###### 0.0233
    sig=5.6704e-8
    Co2_b=params[1] # #### 1.0-0.1904
    Co2_m=params[2] # #### 0.0722
    transmdfactor=params[3] ##### 0.001*0.053
    crit_b=0.71
    crit_m=0.01
    sw_in=341

    transmd=np.exp(-data[:,3]*transmdfactor) #/1000?
    critexp = np.ones(len(transmd))

    B0= (- heatwmsq * (Co2_b - Co2_m * lCo2) *sig)#longwave light

    B1= heatwmsq * sw_in * transmd * (crit_b - crit_m *(1-critexp)) #shortwave light

    def compute_jacobin(x,ki):
        k=int(ki)
        return (1 + B0[k]*4*x**3)

    def compute_constant(x,ki):
```

```
    k=int(ki)
    return (B1[k] + B0[k]*(1)*x**4)
# intial parameters
H=1  #no difference between measurements and model right now
Q = params[4] # process variance 0.001
R = params[5] # estimate of measurement variance, change to see effect 0.007

# allocate space for arrays

xhat=np.zeros(sz)       # a posteri estimate of x
P=np.zeros(sz)          # a posteri error estimate
F=np.zeros(sz)          # Jacobin state transitions
xhatminus=np.zeros(sz)  # a priori estimate of x
Pminus=np.zeros(sz)     # a priori error estimate
K=np.zeros(sz)          # gain or blending factor

xhathat=np.zeros(sz)    # smoothed a priori estimate of x
Phat=np.zeros(sz)       # smoothed posteri error estimate
Khat=np.zeros(sz)       # smoothed gain or blending factor

xblind=np.zeros(sz)

# intial guesses
xhat[0] = 286.6
xblind[0]=286.6
P[0] = 1.0
Pminus[0] = 1.0

z=temps

lml=np.zeros(sz)
y=np.zeros(sz)
qqy=np.zeros(sz)
S=np.zeros(sz)

F[0]=compute_jacobin(286.6,0) #necessary for last step of RTS smoother

for k in range(1,n_iter):
    # time update
    F[k]=compute_jacobin(xhat[k-1],k)


    xhatminus[k] = xhat[k-1] + compute_constant(xhat[k-1],k)
    xblind[k]=xblind[k-1] + compute_constant(xblind[k-1],k)

    Pminus[k] = F[k] * P[k-1]* np.transpose(F[k]) +Q

    # measurement update
    S[k]=H*Pminus[k]*np.transpose(H) +R
    K[k] = Pminus[k]*np.transpose(H)/S[k]
    y[k]=z[k]-H *xhatminus[k]
    xhat[k] = xhatminus[k]+K[k]*y[k]
    P[k] = (1-K[k]*H )*Pminus[k]
    qqy[k]=y[k]/np.sqrt(S[k])
    lml[k]= -0.5* (np.transpose(y[k])/S[k]*y[k] + np.log(S[k]) + np.log(2*np.pi))

xhathat[n_iter-1]=xhat[n_iter-1]
Phat[n_iter-1]=P[n_iter-1]
xhathat[0]=xhat[0]
Phat[0]=P[0]

lsml=0
ybark=0
qqyh=[]

#compute moving averages
N = 30
cumsum, moving_aves = [0], []
for i, x in enumerate(temps, 1):
    cumsum.append(cumsum[i-1] + x)
    if i<N/2:
        moving_aves.append(xhat[0])
    if i>=N:
        moving_ave = (cumsum[i] - cumsum[i-N])/N
        #can do stuff with moving_ave here
        moving_aves.append(moving_ave)

for ik in range(2,n_iter+1):
    # RTS Smoother
    k=n_iter-ik
    # measurement update
    Khat[k] = P[k]*np.transpose(F[k])/Pminus[k] #compute inverse for higher dimensions
    xhathat[k] = xhat[k]+Khat[k]*(xhathat[k+1]- xhat[k] - compute_constant(xhat[k],k))
    Phat[k] = P[k] + Khat[k]*(Phat[k+1]- Pminus[k])*np.transpose(Khat[k])
    if (k<len(moving_aves) and k>N/2):
        ybark= xhathat[k] -moving_aves[k]
        lsml=lsml - 0.5*(np.log(np.abs(Phat[k])) + np.log(2*np.pi) + np.transpose(ybark)/np.abs(Phat[k])*ybark)
        qqyh.append(float(ybark/np.sqrt(np.abs(Phat[k]))))

return (sum(lml)+lsml)/10
```